Subsystem Density Functional Theory for Molecules and Solids: Theory, Development, Applications

by

Alessandro Genova

A dissertation submitted to the

Graduate School – Newark

Rutgers, The State University of New Jersey

In partial fulfillment of the requirements for the degree of

Doctor of Philosophy in Chemistry

written under the direction of

Michele Pavanello

and approved by

Michele Pavanello

Piotr Piotrowiak

Phil Huskey

Neepa Maitra

Newark, New Jersey

May, 2018

Abstract

The Kohn–Sham formulation of density functional theory (KS-DFT) is the most widely employed electronic structure method in the fields of chemistry, physics, and materials science. This is largely due to the fact that KS-DFT produces models of remarkable accuracy and predictive capability with a relatively low computational cost that scales as $O(N^3)$ with respect to the size of system. As researchers strive to simulate larger and more realistic systems, even the convenient scaling of KS-DFT becomes a bottleneck. Subsystem DFT is a popular *divide and conquer* formulation of DFT, where the system is divided into a set of weakly coupled fragments, that is naturally suited for a massively parallel implementations, and has a computational cost that scales linearly with the system size. In this dissertation an extension of subsystem DFT for periodic systems is derived, and a flexible, high performing, massively parallel implementation of the theory is included in a new open-source simulation package: embedded Quantum Espresso (eQE). The applicability of the method is then assessed in several applications, spanning from the interaction between molecules and surfaces, to molecular dynamics of liquids.

Acknowledgements

I would like to take this space to thank the people that accompanied me along this five year long journey.

My largest gratitude debt goes to my advisor, Prof. Pavanello. Thank you Michele for guiding me and for providing me with countless opportunities to improve myself from the beginning of my PhD till the very end. Thank you for your enthusiasm that perfectly balances my skepticism and for putting up with my well known flaws. Thank you for the good times outside the lab as well, at McGovern's, at the parties, and at the Hackathons. I feel extremely lucky to have had you as my advisor, and it has been an honor to be your student at the initial stages of your successful professor career. Thanks to the members of my committee – Prof. Maitra, Prof. Piotrowiak, Prof. Huskey – for finding the time to get interested in my work and to provide insightful comments.

I also want to thank my lab buddies, past and present. Thank you Alisa, Pablo, Rupali, Jaren, Alina, Johannes, Wenhui, for the good times in the office where we'd always find the time to crack a joke or two, for letting me steal all the food, for the drinks together, and the punk-rock shows!

I would like to thank my family – my mom, my dad, Massimo, my brother and my grandparents – for always supporting me over the years, even when the decision to move to a foreign country half way around the world hurt them. I also want to

thank Beyza for being my pillar and for spoiling me especially in this last few stressful months when I most needed it. I'll be there for you when you'll go through the same in a few months.

I also want like to thank the chemistry department, for the financial and logistical support over the year, and Judy in particular.

Contents

List of Figures

List of Tables

Chapter 1

Introduction

Over the past few decades the field of quantum chemistry has achieved remarkable successes in terms of predictive power and applicability. This is in large part due to the improvement of theories such as Kohn-Sham Density Functional Theory (KS-DFT), as well as progress in the computer hardware readily available to researchers.

As we strive for more realistic models, we often need to deal with larger systems that include not only the few molecules we are interested in, but their environment as well. After all, not much of the real world chemistry involves isolated molecules in infinite amounts of vacuum at 0K.

Unfortunately, there are two major issues we need to come to terms when dealing with larger systems. First, even the relatively favorable $O(N^3)$ complexity scaling with respect to the system size of KS-DFT is too expensive for the linear pace at which computers have been progressing. Second, it is difficult to apply our chemical intuition to a large system. Since quantum mechanics does not distinguish between electrons, there is no simple recipe to determine which electron belongs to which portion of the system.

Several partition methods have been proposed to overcome these issues. Central to

all fragment based methods, and to subsystem Density Functional Theory specifically, is the idea that the electron density of a system can be expressed as the sum of the electron densities of arbitrary fragments.

That is

$$\rho(\mathbf{r}) = \sum_{I}^{N_S} \rho_I(\mathbf{r}), \tag{1.1}$$

where ρ_I is the electron density of one of the N_s fragments. The only constraint here is that each of the densities ρ_I integrates to an integer (or fractional) number of electrons N_I, and that the sum of these numbers is equal to the number of electrons N in the system (supersystem, hereafter): $N = \sum_I^{N_S} N_I$.

Eq. 1.1 is the starting point for solving both of the problems above.

For the scaling issue, Eq. 1.1 hints at the fact that we could invoke the principle of *divide-and-conquer*. Splitting the supersystem density does not necessarily lead to faster computations (e.g. in the trivial case of defining the fragment densities by grouping mutually orthogonal orbitals), nor there is a unique way to do it. However, by applying appropriate constraints and approximations, the computational complexity can be highly reduced.

For the interpretative issue, Eq. 1.1 can be used as the starting point to search for the partitioning of a supersystem that provides the highest chemical insight. It is extremely useful to devise methods that can take the coupled electrons in a large molecule and returns information in terms of smaller more tractable fragments[5,57,100] (e.g. functional groups or even individual atoms), and several research groups have successfully explored this direction.[31,55,95,99]

Subsystem Density Functional Theory – also known as Frozen Density Embedding (FDE) – falls into the category of *divide-and-conquer* methods, and it primarily leverages Eq. 1.1 to reduce the computational complexity. The constraint imposed

by FDE is that the overlap between the electron density of different fragments is minimized. This leads to weakly coupled, mostly localized fragments, that can be treated independently from the quantum mechanical point of view, but still influence each other through a so-called *embedding potential*. In nature there are many systems that occur as sets of weakly interacting fragments. For these class of compounds, the subsystem formulation of DFT offers an intuitive description of the underlying physics. In a sense, subsystem DFT has the advantage of both worlds: it is a fast *divide-and-conquer* method, and it also provides results that can be analyzed in an intuitive way.

Practical implementations of subsystem DFT, however, are not immune from limitations. As we will see more in detail later, the approximations introduced to devise a useful practical implementation of FDE, also limit its applicability. FDE cannot be blindly applied to any system. More specifically, care needs to be taken when defining the fragments in the supersystem to ensure that bonds with a covalent character are not shared between subsystems.

Ever since its introduction[134] FDE has been employed as a tool to tackle several problems that would be intractable – either for the computational cost, or for actual limitations of the method – through standard Kohn-Sham DFT. For example, FDE has been employed to constrain spin density on specific fragments,[101,118] to approximate diabatic states involved in charge transfer processes,[102,109,110] or even to estimate van der Waals interactions between different parts of the supersystem.[66]

As its popularity grew, FDE has been included in several quantum chemistry simulation packages. Notable examples of subsystem DFT for molecular system that employ atom centered basis sets are: Amsterdam Density Functional (ADF),[63] TURBOMOLE,[77,78] deMon,[133,135] Dirac,[45] Q-Chem,[47] MolCas.[3]

Historically, FDE has not been as popular in the condensed phase world, but a

few implementations for periodic systems do exist in CP2K,[1,61] ABINIT,[46,50] and CASTEP.[75] However all of these suffer from at least one major limitation such as lacking sampling of the first Brillouin zone or restricting the number of subsystems to two.

This dissertation fills in this gap by creating the most versatile and computationally efficient implementation to date of subsystem DFT for the condensed phase in a plane wave basis.

In chapter 2 details of the general theory of subsystem DFT and its is extension to tackle periodic systems are introduced. In chapter 3 the strategy followed to create the actual implementation in the embedded Quantum Espresso package is explained. In the remaining chapters several successful applications of the method are shown.

In chapter 4 the interaction of molecules and surfaces is modeled. In chapter 5 the locality of subsystem DFT to achieve a more efficient sampling of the first Brillouin zone is exploited. In chapter 6 ab-initio molecular dynamics of liquid water are performed, showing the quality of the method and the efficiency of its implementation.

Chapter 2

The Theory of Periodic Subsystem DFT

This chapter is adapted from the following peer-reviewed paper:

- Alessandro Genova, Davide Ceresoli, and Michele Pavanello. Periodic Subsystem Density-Functional Theory. *J. Chem. Phys.*, 141:174101, 2014

The theory behind periodic subsystem DFT is discussed in this chapter. The goal is to tackle periodic systems, thus the equations derived for practical calculations are generalized to a non-integer subsystem orbital occupation, and to a non-vanishing size of the Brillouin zone.

The fundamental idea behind any subsystem DFT method is that the electron density of the supersystem can be partitioned into the electron densities of the N_S

subsystems, as already shown in 1.1:

$$\rho_{\mathrm{tot}}(\mathbf{r}) \equiv \rho(\mathbf{r}) = \sum_{I}^{N_S} \rho_I(\mathbf{r}) \tag{2.1}$$

The subsystem densities are defined from the orbitals of the corresponding subsystem (for the sake of clarity only the closed-shell case is reported here):

$$\rho_I(\mathbf{r}) = \frac{2}{\Omega_{\mathrm{BZ}}} \int_{\mathrm{BZ}} \mathrm{d}\mathbf{k} \ \sum_j n^I_{j,\mathbf{k}} \left| u^I_{j,\mathbf{k}}(\mathbf{r}) \right|^2 \tag{2.2}$$

where Ω_{BZ} is the volume of the BZ, and $0 \leq n^I_{j,\mathbf{k}} \leq 1$ are the occupation numbers of orbitals belonging to fragment I, and $u^I_{j,\mathbf{k}}(\mathbf{r})$ is such that the Bloch function is $\psi_{j,\mathbf{k}} = e^{i\mathbf{k}\cdot\mathbf{r}} u^I_{j,\mathbf{k}}(\mathbf{r})$. The occupation numbers are formulated such that

$$\sum_j n^I_{j,\mathbf{k}} = N_I \quad \forall \ \mathbf{k} \in \mathrm{BZ}, \tag{2.3}$$

with N_I the number of electrons assigned to subsystem I. The above definition of subsystem density differs from what has been considered in previous formulations of FDE. Here, besides an integral over the BZ, partial orbital occupations are invoked. There are two reasons for this. First a practical one, when tackling metallic systems, due to the continuous density of states at the Fermi energy, the SCF procedure would simply not converge without smearing the occupations across the Fermi energy. Second, when working in a finite temperature regime, the non-pure state resulting from the statistical occupation of excited states can be formally accounted for with a non-integer orbital occupation.[100]

Since the orbitals of one subsystem are not required to be orthogonal to those in another subsystem, complications in the computation of the total non-interacting

kinetic energy arise. We can still define a subsystem non-interacting (Janak) kinetic energy as:

$$T_{\mathrm{J}}[\rho_I] = \frac{2}{\Omega_{\mathrm{BZ}}} \int_{\mathrm{BZ}} \mathrm{d}\mathbf{k} \; \sum_j n^I_{j,\mathbf{k}} \left\langle u^I_{j,\mathbf{k}} \left| -\frac{(\nabla + i\mathbf{k})^2}{2} \right| u^I_{j,\mathbf{k}} \right\rangle \tag{2.4}$$

We are adopting this notation rather than T_s, because the latter is defined for integer occupations only.[100]

As the supersystem total Janak kinetic energy is not simply the sum of the subsystem kinetic energies, it needs to be corrected. Namely,

$$T_{\mathrm{J}}[\rho] = \sum_I T_{\mathrm{J}}[\rho_I] + T^{\mathrm{nad}}_{\mathrm{J}}[\{\rho_I\}] \tag{2.5}$$

The non-additive kinetic energy term is defined as:

$$T^{\mathrm{nad}}_{\mathrm{J}}[\{\rho_I\}] = \tilde{T}_{\mathrm{J}}[\rho] - \sum_I \tilde{T}_{\mathrm{J}}[\rho_I] \tag{2.6}$$

where $\tilde{T}_{\mathrm{J}}$ differs from T_{J} in the fact that it is a pure functional of the electron density. This approach is particularly useful in practical implementations of the method as it allows us to avoid the diagonalization step of the Fock matrix of the supersystem. Thus, the computational bottleneck (in terms of algorithm complexity) is not the Fock matrix diagonalization anymore, but instead is the evaluation of the Coulomb potential. We can also write other energy contributions in a similar fashion:

$$F[\rho] = F[\{\rho_I\}] = \sum_I F[\rho_I] + \tilde{F}[\rho] - \sum_I \tilde{F}[\rho_I] = \sum_I F[\rho_I] + F^{\mathrm{nad}}[\{\rho_I\}], \tag{2.7}$$

where $F[\rho]$ can be any functional of the total electron density, such as the Hartree energy E_H or the exchange–correlation energy E_{XC}.

This trick allows us to write the total energy of the supersystem as the KS-DFT

energies of the single subsystems, plus a contribution arising from the interaction with the other subsystems:[49]

$$E_{\mathrm{FDE}} = \sum_I \left\{ T_{\mathrm{J}}[\rho_I] + E_{eN}^I[\rho_I] + E_H[\rho_I] + E_{XC}[\rho_I] \right\} + \sum_I^{N_S} \sum_{K \neq I}^{N_S} E_{eN}^K[\rho_I] + T_{\mathrm{J}}^{\mathrm{nad}} + E_H^{\mathrm{nad}} + E_{XC}^{\mathrm{nad}} + V_{NN} \tag{2.8}$$

where $E_{eN}^K[\rho_I]$ is the electron–nuclear interaction energy due to the nuclei of subsystem K with the electrons of subsystem I, namely

$$E_{eN}^K[\rho_I] = -\sum_{\alpha \in K} \int \frac{Z_\alpha \rho_I(\mathbf{r})}{|\mathbf{r} - \mathbf{R}_\alpha|} \mathrm{d}\mathbf{r}. \tag{2.9}$$

In addition, V_{NN} is the nuclear repulsion energy.

We obtain the subsystem orbitals by solving self-consistently the following coupled equations:

$$\left[-\frac{1}{2} \left(\nabla + i\mathbf{k} \right)^2 + V_{\mathrm{eff}}^I(\mathbf{r}) \right] u_{j,\mathbf{k}}^I(\mathbf{r}) = \epsilon_{j,\mathbf{k}}^I u_{j,\mathbf{k}}^I(\mathbf{r}). \tag{2.10}$$

In the above equation, as we tackle periodic systems the effective Hamiltonian for periodic systems is invoked which includes the $\mathbf{k}$ vector belonging to the BZ, solving for the periodic part of the Bloch wave. The effective potential V_{eff}^I is given by

$$V_{\mathrm{eff}}^I(\mathbf{r}) = V_{eN}^I(\mathbf{r}) + V_H[\rho_I](\mathbf{r}) + V_{XC}[\rho_I](\mathbf{r}) + V_{\mathrm{emb}}^I(\mathbf{r}), \tag{2.11}$$

and V_{emb}^I appearing above is the so-called embedding potential, which takes the following form

$$V_{\mathrm{emb}}^I(\mathbf{r}) = \sum_{K \neq I}^{N_S} \left[\int \frac{\rho_K(\mathbf{r}')}{|\mathbf{r} - \mathbf{r}'|} \, d\mathbf{r}' - \sum_{\alpha \in K} \frac{Z_\alpha}{|\mathbf{r} - \mathbf{R}_\alpha|} \right] + \frac{\partial \tilde{T}_{\mathrm{J}}[\rho]}{\partial \rho(\mathbf{r})} - \frac{\partial \tilde{T}_{\mathrm{J}}[\rho_I]}{\partial \rho_I(\mathbf{r})} + \frac{\partial \tilde{E}_{XC}[\rho]}{\partial \rho(\mathbf{r})} - \frac{\partial \tilde{E}_{XC}[\rho_I]}{\partial \rho_I(\mathbf{r})}. \tag{2.12}$$

We refer to other review publications[53,62,131] regarding the more profound theoret-

ical ramifications of using the partitioning in Eq. (2.1), and the assumptions related to the non-interacting v-representability of each subsystem density. We will limit ourselves to stating that the more accurate the non-additive KEDF is the closer the FDE results converge to KS-DFT of the supersystem.[62] As the exact functional is unknown, the most important avenue of research in FDE is the systematical improvement of the available KEDF approximants.

A common choice in FDE calculations is to use semi-local GGA KEDF. The general expression for this family of functionals is:

$$\tilde{T}_{\mathrm{J}}^{\mathrm{GGA}} = C_{\mathrm{TF}} \int \rho^{5/3}(\mathbf{r})\, F(s(\mathbf{r}))\, d\mathbf{r} \tag{2.13}$$

where $F(s)$ is the so-called enhancement factor, and s is the reduced density gradient

$$s(\mathbf{r}) = \frac{1}{2(3\pi^2)^{1/3}} \frac{|\nabla\rho(\mathbf{r})|}{\rho^{4/3}(\mathbf{r})}. \tag{2.14}$$

For example, the enhancement factor of revAPBEK (i.e. the functional most often used in the present dissertation) is:

$$F_{\mathrm{revAPBEK}}(s) = 1 + \frac{c_1\, s^2}{1 + \dfrac{c_1}{c_2}\, s^2}, \qquad c_1 = 0.23889, \quad c_2 = 1.245 \tag{2.15}$$

We should remark that the plane wave basis set provides a very efficient mean of calculating the electron–electron repulsion through the solution of the Poisson equation for the corresponding potential in Fourier space. Likewise, the evaluation of the density gradients needed by exchange-correlation and kinetic functionals can also be done in reciprocal space. By exploiting the fast Fourier transform (FFT), this problem is solved with an algorithm that scales as $O(N \log N)$ with N being the

number of plane waves used to span the charge density. In comparison, localized-orbital codes solve the Coulomb problem in real space, offering some advantages with respect to plane waves when the interaction of far-away charge densities is evaluated (i.e., it can be approximated with multipole expansions). However, for computing interactions of close-by charge densities, real-space implementations scale locally as $O(N^2)$ with N being the local set of atomic orbitals.[35,88,111,114]

Chapter 3

Subsystem DFT implementation in embedded Quantum Espresso (eQE)

This chapter is adapted from the following peer-reviewed paper:

- Alessandro Genova, Davide Ceresoli, Alisa Krishtal, Oliviero Andreussi, Robert A. DiStasio Jr., and Michele Pavanello. eQE — A Densitiy Functional Embedding Theory Code For The Condensed Phase. *Int. J. Quantum Chem.*, 117:e25401, 2017

A novel implementation of the FDE method is presented in this chapter. Highlights of this implementation are (1) a proven strong parallel efficiency that consistently outperforms semilocal KS-DFT, (2) the ability to run AIMD, (3) applicability

to periodic systems such as conductors and semiconductors. This new implementation is dubbed embedded Quantum Espresso or eQE,[39] to credit the open-source package Quantum Espresso[43,44] it is based on.

The elements that make eQE unique and extremely efficient are discussed: (1) self-consistency of the electronic structure, (2) guiding the SCF to convergence *via* the introduction of an additional DIIS layer, (3) the employed hierarchical parallelization scheme, (4) sampling of the first Brillouin zone (FBZ), (5) subsystem-specific basis sets, (6) fragment specific spin, and (7) performance.

3.1 Self-consistency of the electronic structure

One key element of the eQE implementation is that we seek a fully self-consistent field (SCF) coherent with the choice of the underlying electronic structure theory. This implies that each subsystem density, ρ_I, needs to be self-consistent as well as converged with respect to variation of the other subsystem densities, $\{\rho_J\}$, for $J \neq I$. To achieve this goal, we have adopted a strategy similar to the one employed in the CP2K implementation of FDE, which prescribes that each subsystem gains knowledge of the other subsystem densities at every SCF cycle.[61] Thus, the KS-like problem in 2.10 is run simultaneously for each subsystem.

The SCF is considered converged once all subsystem density errors from one SCF cycle to the next, σ, are smaller than a user-defined threshold. In our experience, a threshold of $\sigma < 10^{-9}$ Ry is sufficient for running AIMD simulations that achieve a satisfactory energy conservation in the NVE ensemble.

3.2 Guiding the SCF to convergence: an additional DIIS layer

Straightforward implementation of the algorithm described above results in computations that are slower than standard KS-DFT. To achieve a fast and scalable FDE implementation, our efforts began with taking a closer look at the electron density mixing during the SCF procedure. Specifically, we have introduced a new and additional DIIS[107] layer that has substantially decreased the time to solution. Depending on the system, we can achieve a reduction in the number of SCF cycles by up to 50%. This new DIIS layer deals with density mixing at different rates for each of the different subsystems and is applied before the subsystem densities are summed through 2.1 to yield the supersystem density (needed for computing the new potentials for the next SCF cycle).

With $\rho_I^{out}(n_{\mathrm{SCF}})$ we indicate the electron density of subsystem I available in output after SCF cycle n_{SCF} has completed. $\rho_I^{out}(n_{\mathrm{SCF}})$ is mixed with subsystem electron densities of previous SCF cycles employing Broyden density mixing.[16] The density resulting from the Broyden mixing, $\rho_I^{\mathrm{Broyden}}(n_{\mathrm{SCF}})$, is then mixed to the previous SCF density to generate a new density, $\rho_I^{in}(n_{\mathrm{SCF}}+1)$, that will be used to evaluate the KS-DFT potentials of the next SCF cycle, as follows

$$\rho_I^{in}(n_{\mathrm{SCF}}+1) = \beta_I \rho_I^{\mathrm{Broyden}}(n_{\mathrm{SCF}}) + (1-\beta_I)\rho_I^{in}(n_{\mathrm{SCF}}). \tag{3.1}$$

β_I is the Broyden mixing parameter which takes values between 0 and 1. It is typically dependent on the system's gap (i.e., large/small gaps afford large/small β_I).

In the new DIIS method, β_I is made SCF cycle dependent, namely, $\beta_I(n_{\mathrm{SCF}})$, and

it is evaluated in the following way for large values of σ_{FDE},

$$\beta_I(n_{\mathrm{SCF}}) = \beta_I \cdot \max\left\{\frac{\sigma_{FDE}(n_{\mathrm{SCF}}) - \sigma_I(n_{\mathrm{SCF}})}{\sigma_{FDE}(n_{\mathrm{SCF}})}, 0.2\right\}, \tag{3.2}$$

where σ_I is the density difference (or error) with the previous cycle for the subsystem density, and $\sigma_{FDE}(n_{\mathrm{SCF}}) = \max_I \{\sigma_I(n_{\mathrm{SCF}})\}$. While for low values of σ_{FDE} the original β_I is employed.

The effect of this new DIIS layer is such that if one subsystem features large density oscillations from one SCF cycle to the next, its new density will be mixed with the previous ones using a lower mixing parameter (as compared to the other subsystems).

3.3 Hierarchical Parallelization Scheme

The simultaneous solution of 2.10 provides us with the opportunity to task-parallelize eQE at the subsystem level. The subsystem KS equations compute new subsystem densities (e.g., ρ_I) at every SCF cycle, which are then summed to yield the supersystem density (ρ). Given that the density is an array of low dimensionality, its transfer between subsystems involves relatively low data communication traffic.

The first MPI communicator that we define is the `inter_fragment` communicator. This communicator links one selected process for each subsystem (`ionode`, hereafter) and is mostly used for sharing information about the electron density. The `inter_fragment` communicator was inspired by the already existing image parallelization level in QE originally developed for nudged elastic band simulations.[44]

Each subsystem can take advantage of further parallelization. For this we have repurposed the existing `intra_image` communicator (originally developed for NEB

calculations) to collect all processes that are assigned to a subsystem. These processes are further split into pools, in a way that is analogous to the standard QE parallelization architecture.

Figure 3.1 highlights the flexible and hierarchical parallelization strategy employed in eQE. Inset (a) of the figure depicts the parallelization strategy in the native QE code for nudged elastic band simulations. This preexisting strategy is problematic for subsystem DFT approaches, as each subsystem (denoted by the columns in the diagram) is forced to use the same number of processes. This of course is not ideal in those cases in which one subsystem is much larger than the others in terms of the number of valence electrons.

Inset (b) of Figure 3.1 depicts the parallelization strategy in eQE. The clear advantage over the strategy in inset (a) is the fact that the new MPI stack provides us with enough flexibility to assign a *subsystem-specific* number of MPI processes.

The new eQE MPI stack was designed to maximize speed while retaining as much flexibility as possible. For this reason, we also created the MPI communicator `large_comm`, which collects *up to* all available MPI processes to calculate potentials associated with the supersystem density, ρ. For some architectures (*e.g.*, those with relatively slow internode connectivity) the `large_comm` communicator can be disabled by running eQE with the `-nfp` flag, which stands for "no fancy parallelization". Experts can redefine `large_comm` depending on the specific computer architecture and only include the portion of available MPI processes that best exploits the available network architecture.

The number of MPI processes assigned to a given subsystem can be specified in the `fragments_procs.in` file, which needs to be copied into the execution folder before runtime. More specifically, line `n` of `fragment_procs.in` contains the desired number of MPI processes for subsystem `n`.

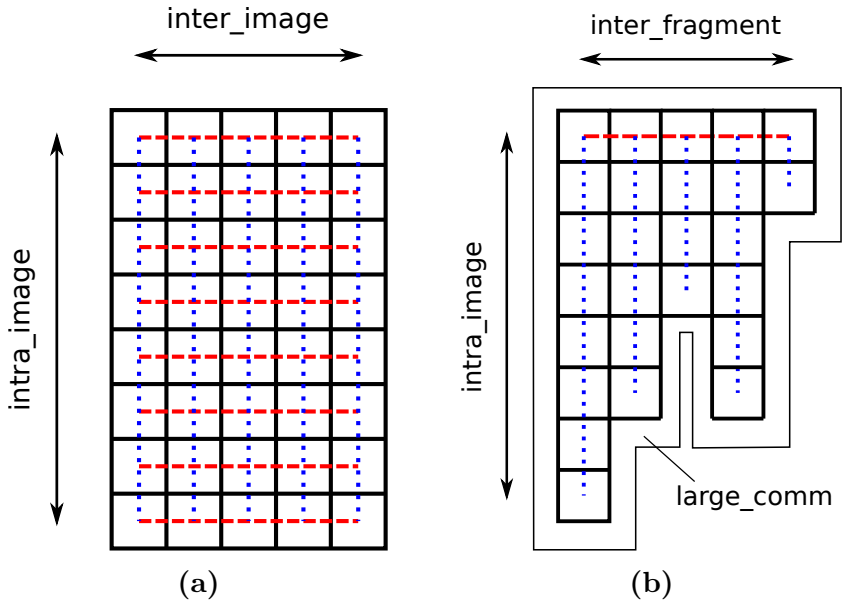

Figure 3.1: Comparison of QE and eQE MPI stacks. Each square represents a single MPI process. Blue dotted segments represent `intra_image` communicators and run along the columns (each representative of a subsystem). The red dashed segments represent communication across subsystems. Inset (a): The original QE MPI stack. All subsystems are restricted to have the same number of processes, and each process is part of a communicator with the corresponding process in the other subsystems (with corresponding topology defined in the `inter_image` MPI communicator). Inset (b): The new eQE MPI stack. The `inter_fragment` MPI communicator links only the first process belonging to each subsystem. As these are important processes, we call them `ionode`. All subsystems are given an arbitrary number of processes (as defined by the repurposed `intra_image` communicator) and the communication *between* subsystems is managed exclusively by the `ionode` set. Distributed quantities, such as densities and potentials, are transmitted across subsystems by first collecting the quantity on each `ionode` (through the `intra_image` communicator corresponding to a given subsystem), broadcasting it across the `ionode` set, and then redistributing it across the `intra_image` communicators. The role of the `large_comm` communicator is to compute potentials corresponding to the supersystem density (*i.e.*, the sum of the subsystem densities) using all available processes.

3.4 Sampling of the First Brillouin Zone (FBZ)

The localized nature of the fragments provided by the theory provides another opportunity to make the solution of the individual fragments more efficient.

In eQE it is possible to assign an independent set of k-points to each subsystem in order to sample the corresponding FBZ, and this number can be chosen according to the nature of the electronic structure of the subsystem. This finding allows us to

represent each subsystem band with the smallest number of k-points needed to reach a target accuracy. Chapter 5 is entirely devoted to this capability of eQE.

3.5 Subsystem-specific basis sets

Another aspect where the true potential of eQE is revealed resides in the definition of subsystem-specific basis sets. Due to the locality of the electronic structure of each subsystem, there is no need to use the entire plane wave set associated with the native simulation cell. Using subsystem based basis sets (also called monomer basis sets in the literature) is an important step for practical implementations of methods that exploit locality, such as subsystem DFT. In the literature, subsystem-based basis set implementations of Frozen Density Embedding are indicated by the acronym FDE(m), while FDE(s) indicates that the supersystem basis set is used for all subsystems.[63] While achieving this goal is (at least on paper) relatively straightforward when atom-centered basis sets are employed, the fact that QE includes periodic boundary conditions and employs an originless plane-wave (PW) basis set, presents us with a challenge. If all of the N_S subsystems are represented on the same supersystem simulation cell and share the same kinetic energy cutoff in the PW expansion, the code would thus need to solve N_S coupled KS-like problems in the large (supersystem) basis set. This would significantly slow down the procedure even when compared to semilocal KS-DFT for the supersystem and defeat the purpose of using the subsystem approach. Hence, one way to employ subsystem-specific basis sets is to define smaller simulation cells whose PWs (the number of which is significantly reduced compared to the set associated with the native supersystem cell) are employed in the expansion of the subsystem orbitals or bands (see Figure 3.2).

To achieve this goal, in eQE smaller and subsystem-centered cells are "carved out" of the native cell and used only to expand the subsystem molecular orbitals (*i.e.*, bands or waves). The cells are allowed to overlap so that the nonadditive potentials can be computed with no loss of accuracy.

In eQE, each subsystem lattice vector can be scaled independently from the others by assigning a value less than 1.0 to the keyword `fde_cell_split(n)`, with `n=1, 2, 3`. The subsystem cells are then generated by scaling the three lattice vectors of the supersystem cell by the values of `fde_cell_split(n)` in such a way that the grid points of each subsystem cell are imposed to match exactly with corresponding points in the supersystem cell. This allows us to efficiently (and exactly) transfer density and potentials in real space back and forth between the subsystem and supersystem cells rather than performing more expensive (and less accurate) interpolation schemes. As an illustrative example of how the subsystem cell approach is employed in eQE, consider the computation of the total electron density. This fundamental task in subsystem DFT is computed through 2.1.

Iterative schemes to diagonalize the Hamiltonian for a few selected roots only (*i.e.*, Lanczos-based approaches) are commonly employed in condensed-phase SCF algorithms and their complexity is proportional to the square of the simulation cell volume. As such, it is immediately clear that the subsystem-specific simulation cell (or subsystem-specific basis set) approach described above allows for a significant reduction in the computational cost and scaling of the diagonalization routine (see Section "Applicability and performance of eQE" for timings that compare the supersystem versus subsystem-specific basis set).

There are many types of condensed-phase systems for which such a subsystem specific cell approach is useful. For example, simulations of molecular liquids, such as water, have been carried out (see Chapter 6 and Figure 3.2). Generally speaking,

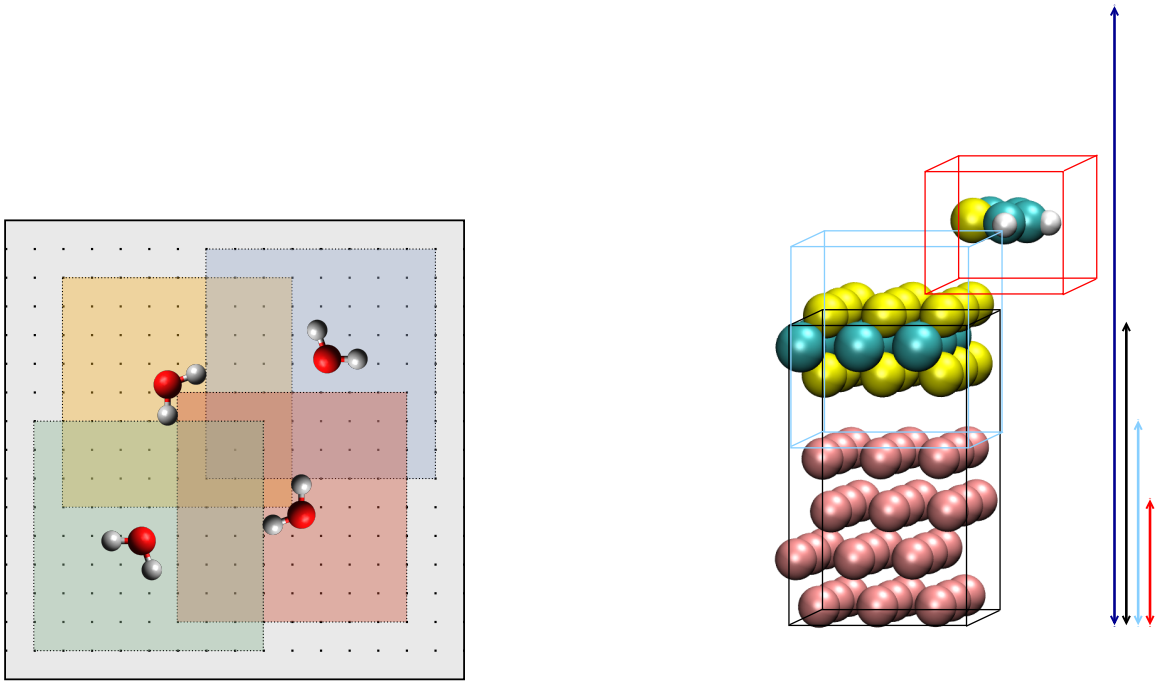

(a) **(b)**

Figure 3.2: Graphical depiction of the scheme utilized for handling the PW expansion of subsystem molecular orbitals. Small, subsystem-centered cells are "carved out" of the supersystem cell and used to expand the subsystem molecular orbitals only. The subsystem cells are allowed to overlap so that the nonadditive potentials can be computed accurately. To ensure grid point matching in the subsystem and supersystem cells, there are some constraints in the choice of the scaling factors, `fde_cell_split(n)`. Inset (a) depicts liquid water, a system made of non-periodic subsystems, while inset (b) depicts a system composed of two stacked slabs and an adsorbate. For (b) the cells of the periodic subsystems (Au and MoS_2) can be reduced along the z-direction. The arrows in (b) depict the relative lengths of the various cells with the longest being associated with the supersystem cell.

the subsystem-specific cell approach is useful in cases where the periodicity of a subsystem is less than or equal to two dimensions. The case of slabs is important as the simulation cell can be reduced in the vertical direction, effectively reducing the amount of vacuum that needs to be considered in the molecular orbital expansion and therefore speeding up the calculation considerably.

3.6 Subsystem-specific spin

One of the aims of an embedding code is to be able to treat radical species in general environments that can be either open- or closed-shell. Thus, eQE has been designed to provide this flexibility and allows one to treat closed-shell subsystems embedded in open-shell environments and vice versa.[41] This is achieved using two keywords: `fde_nspin` and `nspin`. The general case has an open-shell supersystem density, achieved with `fde_nspin=2`, while the spin of the individual subsystems can be set as either closed- or open-shell by setting `nspin` to 1 or 2, respectively. Non-collinear spin options are not yet supported in eQE.

3.7 Performance

To test the performance and the parallel scalability of eQE we considered a few large systems. We focused on molecular liquids, solvated molecules, and molecular crystals.

First we considered $(H_2O)_{256}$ to see how eQE performs in absolute terms compared to KS-DFT, and to check its parallel potential (i.e. the speedup obtained when more processors are added to the same calculation). The findings are reported in Table 3.1 and Figure 3.3. The main conclusion here is that eQE performs about four times faster than semilocal KS-DFT for this system when 256 MPI processes are employed and the parallelization scheme is optimized (all calculations are carried out on 256 CPUs distributed across nodes of dual 10-core E5-2680v2 Ivy Bridge 2.80 GHz processors). Figure 3.3 further shows that eQE is better able to utilize a larger number of employed processes than QE (*i.e.*, a more favorable strong scaling performance), widening the gap with KS-DFT in the large process limit.

Table 3.1: Computational timings for an eQE calculation on $(H_2O)_{256}$ as compared to supersystem-based semilocal KS-DFT in QE. All 256 subsystems were computed at the Γ-point. eQE[1]: Fully optimized eQE employing subsystem specific basis sets, and calculating the GGA xc and kinetic potentials of the total density only once on the supersystem cell utilizing the `large_comm` communicator (*i.e.*, "fancy parallelization"). eQE[2]: GGA xc and kinetic potentials of the supersystem density are computed independently by each subsystem on the small, subsystem-specific cells with the `intra_image` communicator. eQE[3]: In addition to eQE[2], the "no fancy parallelization" flag, `-nfp`, is invoked (*i.e.*, no use of `large_comm`). eQE[4]: In addition to eQE[3] the supersystem PW basis is employed to expand the KS orbitals of each subsystem, predictably further slowing down the calculation.

	eQE[1]	eQE[2]	eQE[3]	eQE[4]	KS-DFT
Speedup	4.1×	2.9×	1.9×	0.1×	1.0×
Time / SCF cycle (s)	115	161	242	4500+	469

We have also investigated the efficiency of eQE compared to standard KS-DFT in QE for three large-scale condensed-phase systems of interest, each containing over 1000 atoms: (1) Molecular Liquids *via* bulk liquid water represented by 1024 independent water molecules (containing 3072 atoms, see Figure 3.4(a)), (2) Polypeptide/Biomolecule Solvation *via* $(GLY)_6$ solvated in $(H_2O)_{395}$ (containing 1230 atoms, see Figure 3.4(b)), and (3) Molecular Crystals *via* a 3×3×3 periodic supercell of pentacene (containing 1940 atoms, see Figure 3.4(c)).

In Table 3.2, we report the computational timings for these three large-scale condensed-phase systems. The most important aspect of this data is that eQE surpasses KS-DFT by more than one-order-of-magnitude for all of these realistic condensed-phase systems. In addition, we note that different systems feature different levels of speedup. This is because the subsystems have different sizes in these three cases (*e.g.*, pentacene is a large molecule compared to water). Generally speaking, eQE will be less efficient if any of the subsystems approach the size of the supersystem simulation cell.

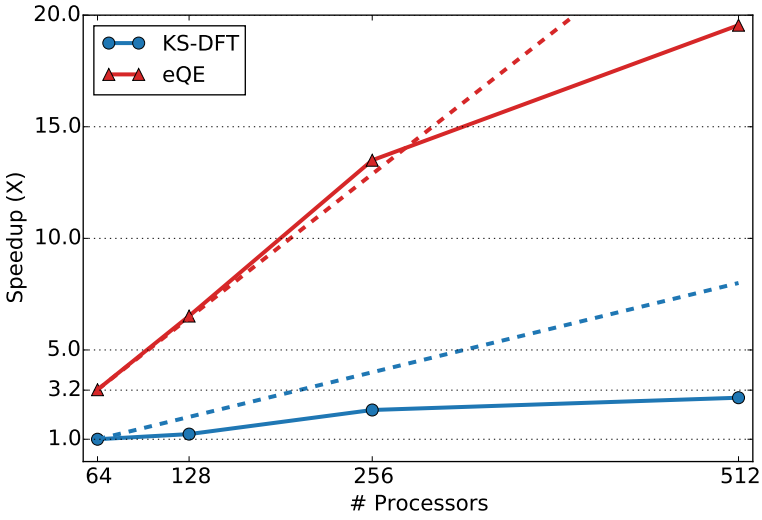

Figure 3.3: Strong parallel scaling of eQE for a system composed of 256 water molecules as a function of the number of MPI processes employed. The dashed lines represent the ideal speedups for eQE (red) and supersystem KS-DFT (blue). The 1.0× reference corresponds to the supersystem KS-DFT baseline on 64 MPI processes.

Table 3.2: Computational timings for eQE calculations on the three large-scale condensed-phase systems in Figure 3.4. Timings are compared against semilocal KS-DFT of the supersystem and refer to the total CPU time needed to perform 10 steps of AIMD (except for the liquid water system). For $(H_2O)_{1024}$, the speedup was evaluated for the first 10 SCF cycles only (as we were unable to converge the SCF with KS-DFT in this system despite a tremendous amount of effort).

System	# of Atoms	Time eQE[1] (s)	Time KS-DFT (s)	Speedup
$(H_2O)_{1024}$	3072	115	2917	25.3×
$(\text{GLY})_6$ in $(H_2O)_{395}$	1230	1462	56405	38.6×
Pentacene $3 \times 3 \times 3$	1940	7156	85718	12.0×

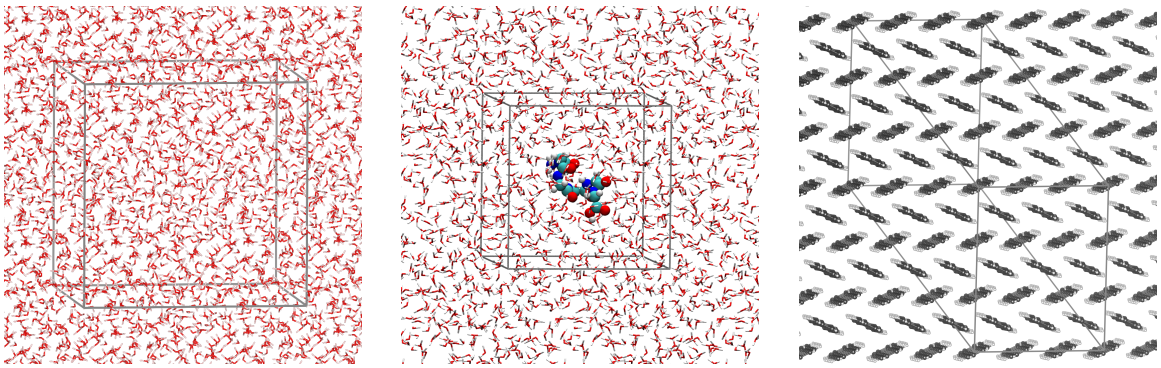

(a) Molecular Liquids **(b)** Biomolecule Solvation **(c)** Molecular Crystals

Figure 3.4: Graphical depictions (to scale) of three large-scale condensed-phase systems employed to investigate the efficiency of eQE. (a): Bulk liquid water represented by 1024 independent water molecules. (b): $(\text{GLY})_6$ solvated in $(H_2O)_{395}$ (c): A 3×3×3 periodic supercell of pentacene.

Chapter 4

Subsystem DFT simulations of molecules and solids

This chapter is adapted from the following peer-reviewed paper:

- Alessandro Genova, Davide Ceresoli, and Michele Pavanello. Periodic Subsystem Density-Functional Theory. *J. Chem. Phys.*, 141:174101, 2014

The applicability of eQE in conjunction with standard GGA nonadditive kinetic energy functionals is assessed in this chapter. An array of different interactions are considered, spanning from simple molecular dimers, to more complicated systems such as multiple molecules adsorbed on a metal surface.

All the calculations (KS-DFT and FDE) have been performed with eQE. We have used Ultrasoft pesudopotentials from the original QE library and from *GBRV*[38] library. The plane wave cutoffs are 40 Ry and 400 Ry, for the wave functions and den-

sity, respectively. Unless stated otherwise, the PBE[105] functional has been employed for the exchange-correlation, and either the LC94[80] or revAPBEK[77] functionals have been employed as non-additive KEDFs.

Regarding the sampling of the BZ, in the calculations invoving molecular systems we have only sampled the Γ point, while for periodic systems we have used the Monkhorst–Pack[92] sampling with a $2\times2\times1$ mesh. In addition, we used a Methfessel–Paxton smearing[91] with 1×10^{-2} Ry of smearing parameter. The smearing was only applied to the metallic subsystems, whereas the molecular subsystems were treated with integer orbital occupations. The structures, cell dimensions, and energy cut-offs can be found in the supplementary materials.[32]

We have benchmarked FDE calculations against KS-DFT references by comparing physisorption energies and corresponding electron densities obtained with the two methods. The simulations consist of single point calculations with the same geometry for both KS-DFT and FDE (e.g. the equilibrium geometry of the system calculated with KS-DFT with exception of the 2PDI on Au). Moreover, a more insightful comparison is made by calculating the number of electrons misplaced by FDE, $\langle\Delta\rho\rangle$, defined as:[64,70]

$$\langle\Delta\rho\rangle = \frac{1}{2}\int |\Delta\rho(\mathbf{r})|\, d\mathbf{r} \tag{4.1}$$

where

$$\Delta\rho(\mathbf{r}) = \rho_{\mathrm{FDE}}(\mathbf{r}) - \rho_{\mathrm{KS}}(\mathbf{r}) \tag{4.2}$$

$\langle\Delta\rho\rangle$ is an important quantity, as it vanishes only when FDE and KS-DFT electron densities coincide. As $\langle\Delta\rho\rangle$ is a size-sensitive quantity, we always compare it to the total number of subsystems and the total number of electrons, as well as the $\langle\Delta\rho\rangle$ arising from the sum of the isolated fragment densities

4.1 Results

We have chosen a set of molecular systems (water dimer and ammonia borane) as well as molecules on metal surfaces (CH_4 on Pt, water on Pt and perylene diimide on Au) as our set of pilot calculations. The goal of the calculations involving the molecular systems is to show that our FDE implementation reproduces the already reported behavior of FDE for these systems. Generally, FDE delivers results close to KS-DFT when the inter-subsystem density overlap is low. Thus, water dimer is expected to be well described by FDE, while for the ammonia borane system, due to the partial charge transfer and covalent character of the B–N dative bond, FDE is expected to fail. We will show that when tackling molecules adsorbed on surfaces, similar considerations to the molecular case apply. I.e. the larger the density in the region between subsystems, the less accurate FDE will be.

4.1.1 H_2O dimer

The first system we used to benchmark our FDE code is the water dimer, with the two water molecules arranged to form a single hydrogen bond, see Figure 4.1a.

It has been shown in previous publications[49,61,130] that FDE implementations with localized basis are capable of obtaining accurate results for this system when a GGA KEDF is employed for the non-additive kinetic energy part. We have calculated an attractive interaction energy of 4.317 kcal/mol with regular KS-DFT, while FDE overestimates this energy by about 0.3 kcal/mol and, in this particular case, is well within 1 kcal/mol threshold.

The very good agreement between between KS-DFT and FDE for the interaction energy is also reflected in the number of misplaced electrons $\langle \Delta\rho \rangle$. As reported in Table 4.2 only 2.85×10^{-2} (2.91×10^{-2}) electrons out of 16 have been displaced

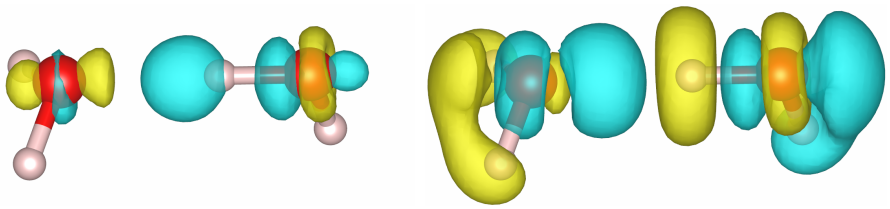

(a) **(b)**

Figure 4.1: Water dimer. a: Difference between the FDE density and the KS density; b: Difference between the sum of the densities of isolated fragments and the KS density. In both cases a 1×10^{-3} isosurface is plotted.

by the selfconsistent FDE calculation using the LC94 (revAPBEK) functional: this represents a 72% improvement over the sum of the isolated fragments densities. In Figure 4.1a the difference between the FDE and KS-DFT densities as defined in Eq. (4.2), $\Delta\rho(\mathbf{r})$, is plotted. The figure shows that the FDE method localizes too much density on the oxygen lone pairs in turn depleting of electron density the hydrogen bond between the two dimers. As a reference, Figure 4.1b reports the difference between the KS-DFT density of the dimer and the sum of the density of the two isolated fragments. Using the same isosurface we can see that the difference is much larger than that of FDE, as has already been shown quantitatively in Table 4.2. Thus, we conclude that for this system FDE performs very well, recovering almost exactly the same electronic structure obtained with a KS-DFT calculation.

4.1.2 Ammonia Borane

As shown previously,[37] the ammonia borane complex is expected to represent a challenge for FDE. It is a Lewis acid-base complex that exhibits a partial charge transfer from the ammonia lone pair to the borane, yielding a so-called dative bond characterized by a dissociation energy of 34.783 kcal/mol as calculated by us using KS-DFT, in good agreement with coupled cluster calculations.[8] The FDE interaction energy of 80.865 kcal/mol and 82.468 kcal/mol significantly overestimates the refer-

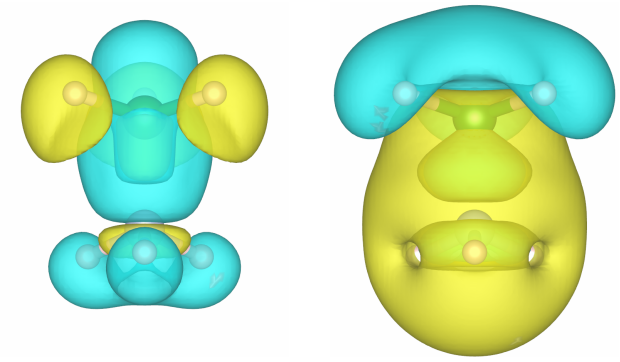

(a) **(b)**

Figure 4.2: Ammonia borane complex. Borane on top. a: Difference between the FDE density and the KS density; b: Difference between the sum of the densities of isolated fragments and the KS density. In both cases a 1×10^{-3} isosurface is plotted.

ence when using LC94 or revAPBEK non-additive KEDF, respectively.

More important is the analysis of the electron density: the difference between the FDE density (and superposition of the isolated fragments densities) with the supersystem KS-DFT density is reported in Figure 4.2a (Figure 4.2b). As the electron density undergoes significant changes upon formation of the complex, FDE only qualitatively reproduces the KS-DFT density – there is a general underestimation of electron density along the B-N bond, while the hydrogens bonded to N (B) are too acidic (basic). Similar results are obtained from localized basis implementations of FDE.[37]

Quantitatively, the number of electrons misplaced by FDE in our calculations is 1.940×10^{-1} and 1.981×10^{-1} when employing the non-additive KEDF LC94 and revAPBEK, respectively. Despite this we can see from Table 4.2 that FDE yielded a good 58% improvement in the density over the sum of the isolated fragments. In conclusion, we confirm previous FDE calculations of this complex[37] and we also show that our plane wave implementation maintains quantitatively the FDE electronic structure predicted by atomic orbital based implementations.

4.1.3 CH_4 on Pt(100)

Catalytic activation of methane by adsorption on a transition metal surface represents an interesting problem, as it could represent a cheap way to produce hydrogen, or a precursor in the synthesis of more complex organic compounds.

On a Pt(100) surface methane can be adsorbed on several sites, so-called top, bridge, and hollow. In addition the molecule can have several configurations with respect to the surface. We have tested the behavior of FDE against the 8 configurations shown in figure 4.3.

As it has been observed in Ref.[94] and confirmed in our calculations (Table 4.1) the CH_4-Pt interaction is generally very weak, and the potential energy surface is relatively uncorrugated (i.e. insensitive to the methane orientation). The only clear potential well is represented by the T1 configuration, which has an interaction energy about 0.5 kcal/mol higher than all the others. From an analysis of the local density of states of this configuration, it has been concluded that in the T1 case we are dealing with a real chemisorption (electron backdonation from the the metal d orbitals to the carbon), rather than a physisorption (polarization of the metal-methane electron densities).[94]

We can see that when using the revAPBEK functional FDE reproduces the supersystem KS calculation in an accurate way for all configurations but T1 and to a lesser extent H1: the small interaction energies are generally slightly understimated, and the number of displaced electrons is very small, ranging from 1.5×10^{-2} to 2.5×10^{-2}, which accounts to a 13% to 32% improvement over the density of the sum of fragments. The FDE results using the LC94 functionals are generally not as good as those with the revAPBEK functional for this system: we can see from Table 4.2 that LC94 yielded little to no improvement over the sum of the fragments.

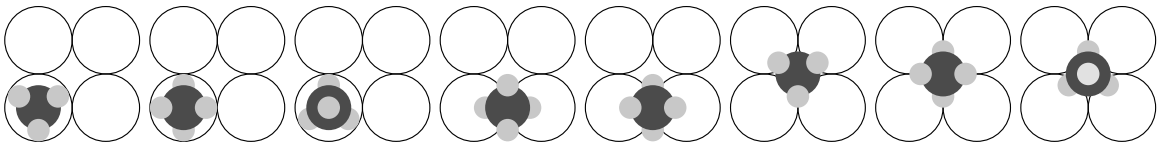

(a) T1 **(b)** T2 **(c)** T3 **(d)** B2a **(e)** B2p **(f)** H1 **(g)** H2 **(h)** H3

Figure 4.3: Configurations of methane adsorbed on Pt(100) considered in the calculations.

It is important to point out that the sum-of isolated-fragments approach is not self-consistent with respect to the interaction between the fragments. Thus, the fact that FDE's self-consistent density agrees with KS-DFT and with KS-DFT and with the sum-of-fragments indicates that FDE's effective potential (i.e. the non-additive potentials) behave physically for physisorption interactions.

As expected the T1 configuration is the one for which FDE yielded the worst results, because of the chemical nature of the bond between the hydrocarbon and the surface: we can see that FDE predicts a small repulsive interaction, equal to 1.302 kcal/mol for LC94 and 0.987 kcal/mol for revAPBEK, whereas KS has an attractive energy of 1.823 kcal/mol. The number of electrons misplaced $\Delta\rho$ is about 9×10^{-2}, which is much higher than what abserved for all the other configurations, and offers no improvement in the prediction of the density over the sum of the isolated fragments. In Figure 4.4, an isosurface plot of $\Delta\rho(\mathbf{r})$ for the T1 configuration is reported. Again, we see that the selfconsistent FDE density is smaller than the KS-DFT one in the interfragment bonding region.

4.1.4 H_2O on Pt(111)

The most complex system we have used to benchmark this periodic implementation of FDE is a water bilayer adsorbed on a Pt(111) surface. The system consists of 13 fragments, 12 water molecules plus the metal surface. The geometry we have employed to model the water bilayer is the so-called *RT3*, as described in Refs.[29,90]

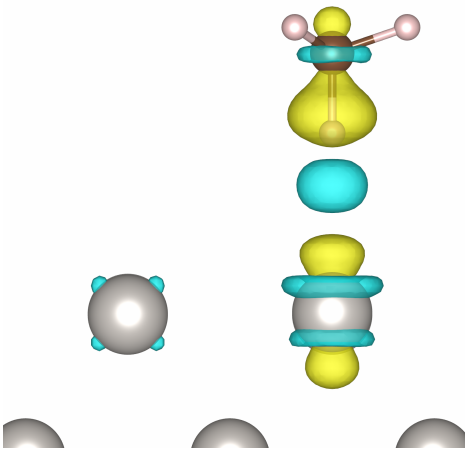

Figure 4.4: Methane on Pt $\Delta\rho(\mathbf{r})$ 0.001 isosurface plot. Yellow identifies positive regions (excess of FDE density), blue identifies negative regions (excess of KS density).

On the layer closer to the surface, we can distinguish between two kinds of water molecules: the ones with the dipole moment parallel to the metal surface, and the ones with a non-zero dipole component perpendicular to the surface. The intermolecular interactions playing an important role in keeping the the bilayer and the metal together are three: (1) the hydrogen bonds network, (2) the interaction between the surface and the parallel dipole water molecules, and (3) the interaction between the surface and the water molecules having non-zero perpendicular component of the dipole.

We have already seen in Section 4.1.1 that FDE describes well hydrogen bonds. This system, however, will probe the ability of FDE to describe the other two cases. Thus, we have run two additional simulations:

1. A single parallel water molecule adsorbed on the surface;

2. A single non-parallel water molecule adsorbed on the surface;

In both cases the position of the molecule is the same as that in the bilayer, without performing any additional optimization. Below we will describe separately these two additional calculations and the one pertaining the full bi-layer.

Table 4.1: Results summary Table # 1. For each system studied, we have calculated the interaction energy at the KS-DFT level and at the FDE level (using the LC94 and revAPBEK kinetic energy functionals).

	Int. En. KS (kcal/mol)	**Int. En. LC94** (kcal/mol)	**Int. En. rAPBEK** (kcal/mol)
H_2O Dimer	−4.32	−4.65	−4.47
BH_3−NH_3	−34.78	−80.87	−82.47
CH_4 on Pt T1	−1.82	+1.30	+0.99
CH_4 on Pt T2	−1.38	−0.49	−0.69
CH_4 on Pt T3	−1.37	−0.49	−0.69
CH_4 on Pt B2a	−1.37	−0.43	−0.60
CH_4 on Pt B2p	−1.31	−0.61	−0.71
CH_4 on Pt H1	−1.27	−0.55	−0.73
CH_4 on Pt H2	−1.31	−0.54	−0.65
CH_4 on Pt H3	−1.35	−0.54	−0.64
H_2O on Pt ($\parallel$)	−3.17	+0.04	+0.07
H_2O on Pt ($\perp$)	−0.52	−0.16	+0.05
12 H_2O on Pt	−135.47	−122.59	−117.82
2 PDI on Au	+8.68	−17.08	−16.06

Parallel H_2O

For the parallel water molecule, KS predicts an adsorption energy of 3.168 kcal/mol while according to FDE the molecule is unbound, with an adsorption energy very close to zero, see Table 4.1.

This discrepancy is also reflected in the number of misplaced electrons $\Delta\rho$, that for this system is the highest so far and equal to 1.643×10^{-1}. Plots of $\Delta\rho(\mathbf{r})$ in Figure 4.5a show that once again FDE places too much density on the oxygen lone pairs and not enough in the bonding region between the molecule and the surface. Despite this, we can see from Table 4.2 that with respect to the sum of fragments FDE managed to recover a good 41% of the change in the electron density due to the interaction between the molecule and the surface.

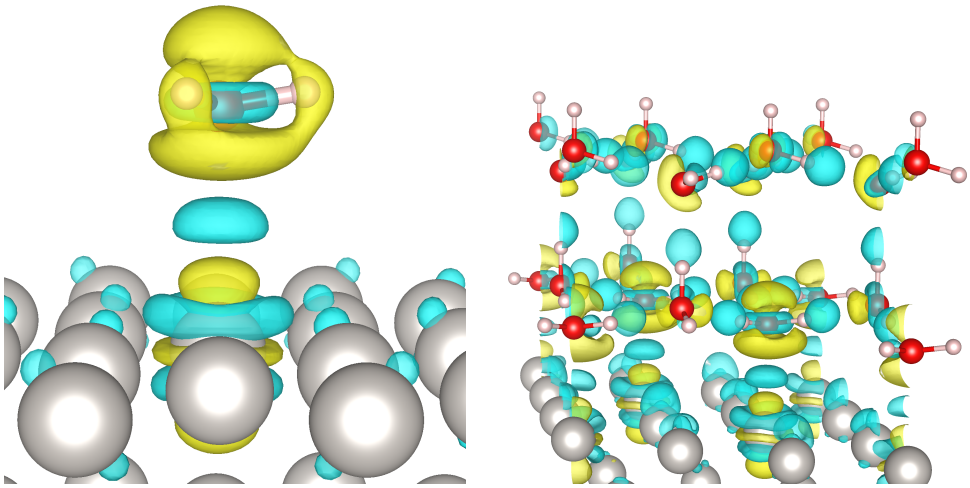

(a) (b)

Figure 4.5: Water on Pt a and water bilayer on Pt b $\Delta\rho(\mathbf{r})$ 0.001 isosurface plot. Yellow identifies positive regions (excess of FDE density), blue identifies negative regions (excess of KS density).

Perpendicular H_2O

The non-parallel water molecules are further from the surface, and interact with it weakly, 0.523 kcal/mol as predicted by KS, and 0.162 kcal/mol according to FDE. FDE has no problems recovering the same total density as KS, with only 1.62×10^{-2} electrons displaced. The electrons displaced by considering the sum of fragments, 8.2×10^{-2} is surprisingly high, for a supposedly almost non interacting system. As reported in Table 4.2 FDE yields a 80%-84% improvement in the quality of the electron density over the sum of the fragments, marking an achievement of the method.

Water Bilayer

As we have seen in the previous sections, we expect that for the bilayer the largest source of error is due to the water molecules in the first layer parallel to the surface and to a lesser extent due to the hydrogen bond network.

The total intermolecular interactions as predicted by KS-DFT is 135.147 kcal/mol, while FDE underestimates it by about 10% yielding an interaction equal to 122.594 kcal/mol

(117.82 for revAPBEK). As shown in Table 4.2 only 6.4×10^{-1} out of the total 368 are misplaced by FDE in this complex 13 fragments system. This represents a 62% improvement over the 1.66 electrons misplaced by the sum of the isolated fragments. An isosurface plot of $\Delta\rho(\mathbf{r})$ is presented in Figure 4.5b. In the figure we see that the expected maximum discrepancy between the KS-DFT and FDE densities is in the bond between the parallel water molecules and the surface, as well as in the many hydrogen bonds keeping the bilayer together.

4.1.5 Perylene Diimide on Au(111)

Perylene diimides (PDIs) are a class of compounds whose electron-accepting character and charge transport properties make them useful materials in the design of new photovoltaic cells based on organic compounds.

We have run a single point KS simulation of two N,N'-dihydro perylene diimides stacked on top of a Au surface. The geometry has been optimized at the KS-DFT level constraining the PDI–PDI distance and the PDI–Au distance to be 3 Å.

From the KS-DFT calculation of the supersystem, it has been predicted a 8.678 kcal/mol repulsive interaction energy. The positive sign in the interaction energy is not surprising since van der Waals (vdW) forces are the most important intermolecular forces in this case, and it is known that KS-DFT calculations employing semilocal GGA exchange–correlation functionals are generally unable to recover them.

Conversely, FDE predicts an attractive interaction energy of 17.078 kcal/mol and 16.064 kcal/mol with LC94 and revAPBEK, respectively. Despite not reproducing the KS-DFT interaction energy, this result is correctly attractive. Such a behavior from FDE has been reported previously,[12,65,66] and in addition recently it was shown that when the FDE interaction is corrected adding a van der Waals term (either through

Table 4.2: Results summary Table # 2. For each system studied number of electrons that has been displaced by FDE with respect to the KS reference, and the electrons displaced if we just consider the density from the sum of the isolated fragments. The column with the percentages represents the improvement of FDE over the sum of the fragments with the following scale: +100% is perfect agreement with KS, 0% is no improvement over the density arising from the sum of the isolated fragments.

	$\langle\Delta\rho\rangle \sum$ **Frag.**	$\langle\Delta\rho\rangle$ **LC94**		$\langle\Delta\rho\rangle$ **rAPBEK**	
H_2O Dimer	0.103	0.028	+72%	0.029	+72%
$BH_3{-}NH_3$	0.462	0.194	+58%	0.198	+57%
CH_4 on Pt T1	0.086	0.092	−7%	0.090	−5%
CH_4 on Pt T2	0.031	0.029	+6%	0.025	+20%
CH_4 on Pt T3	0.026	0.024	+11%	0.018	+32%
CH_4 on Pt B2a	0.027	0.028	−4%	0.024	+13%
CH_4 on Pt B2p	0.029	0.028	+2%	0.023	+20%
CH_4 on Pt H1	0.026	0.032	−21%	0.029	−9%
CH_4 on Pt H2	0.025	0.026	−4%	0.022	+14%
CH_4 on Pt H3	0.021	0.021	+1%	0.016	+28%
H_2O on Pt ($\parallel$)	0.276	0.164	+41%	0.163	+41%
H_2O on Pt ($\perp$)	0.082	0.016	+80%	0.014	+84%
12 H_2O on Pt	1.676	0.649	+61%	0.642	+62%
2 PDI on Au	0.576	0.341	+41%	0.388	+33%

pair-wise additive corrections,[12] or through RPA-like theories[66]) the interaction energy is well-positioned compared to benchmark values.

Regarding the quality of the electron density, as reported in Table 4.2, the number of displaced electrons is 3.4×10^{-1} with LC94 and 3.9×10^{-1} with revAPBEK – an improvement of 41%-33% over the sum of the isolated fragments.

Chapter 5

Efficient sampling of the first Brillouin zone

This chapter is adapted from the following peer-reviewed paper:

- Alessandro Genova and Michele Pavanello. Exploiting the Locality of Subsystem Density Functional Theory: Efficient Sampling of the Brillouin Zone. *J. Phys.: Condens. Matter*, 27:495501, 2015

The partitioning of a supersystem into many independent Kohn-Sham subsystems is exploited further in this chapter. Each subsystem can be treated as its own electronic structure problem with subsystem-specific choices of certain descriptors, and a particular focus is given to the sampling of the First Brillouin Zone (FBZ).

Sampling of the FBZ arises in periodic system because the Hamiltonian is invariant to any lattice translation $\mathbf{T}(\mathbf{n})$ (i.e. the potential has the same periodicity as the

system). Thus, it follows that

$$[H, \mathbf{T}(\mathbf{n})] = 0, \tag{5.1}$$

and the eigenstates of the Hamiltonian can be chosen to be eigenstates of the lattice translation operator as well. This leads to the Bloch theorem,[13] that states that solutions of a periodic Hamiltonian assume the form

$$\psi_{i,\mathbf{k}}(\mathbf{r}) = e^{i\mathbf{k}\cdot\mathbf{r}}\, u_{i,\mathbf{k}}(\mathbf{r}) \tag{5.2}$$

where $u_{i,\mathbf{k}}(\mathbf{r})$ is a function with the same periodicity of the system.

Therefore eigenstates of the periodic Hamiltonian are labeled by two quantum numbers, a band number n, and a vector belonging to the reciprocal space $\mathbf{k}$. Furthermore, being the Hamiltonian block diagonal with respect to different $\mathbf{k}$ vectors, its solutions can be found separately for each given $\mathbf{k}$ within the FBZ.

By imposing Born–Von-Karman boundary conditions we know that there are an equal number of possible $\mathbf{k}$ vectors in the FBZ as the number of unit cells in the crystal, making the discrete $\mathbf{k}$ vectors in principle extremely dense in the FBZ. Because of this, it follows that for periodic systems the evaluation of many properties of interest will lead to integrals over the full FBZ. For example, the electron density, $\rho(\mathbf{r})$, is built from the Kohn–Sham (KS) orbitals, $\psi_{i,\mathbf{k}}(\mathbf{r})$, as

$$\rho(\mathbf{r}) = \frac{1}{\Omega_{\mathrm{FBZ}}} \sum_i \int f(\mathbf{k}, i)\, \psi^*_{i,\mathbf{k}}(\mathbf{r}) \psi_{i,\mathbf{k}}(\mathbf{r}) d\mathbf{k} \quad , \tag{5.3}$$

where $f(\mathbf{k}, i)$ is a continuous function of $\mathbf{k}$ associated with the occupation number of the i-th band.

A great deal of work has been put into developing general ways of finding the smallest possible set of $\mathbf{k}$ points that would still yield accurate results.[6,14,22,33,92,93,113]

By doing so the integral over the FBZ is approximated by a finite sum over the chosen set of **k** points:

$$\frac{1}{\Omega_{\mathrm{FBZ}}}\int_{\mathrm{FBZ}} d\mathbf{k} \quad \rightarrow \quad \sum_{\mathbf{k}} w_{\mathbf{k}} \tag{5.4}$$

where $w_{\mathbf{k}}$ represents the integration weight of each point.

The **k**-point sampling is heavily system dependent. Metals require large sets of **k** points, while a simulation of insulators or semiconductors can be just as accurate with a smaller subset of **k** points.

Isolated molecules and aperiodic systems[87] in general behave differently: if we imagine a three-dimensional periodic array of identical molecules, each in a unit cell much larger than the molecule itself, we can expect the electron density of each molecule to decay to zero well before overlapping with the electron density of a periodic image. We could then perform the trivial exercise of building the tight-binding model of such system according to which the basis functions centered on each lattice point $\mathbf{R}_a$ are the solution of the molecular Hamiltonian $\phi_m(\mathbf{r}-\mathbf{R}_n) \equiv |m,\mathbf{R}\rangle$ where $H^{\mathrm{mol}}\,|m,\mathbf{R}\rangle = E_m\,|m,\mathbf{R}\rangle$. Since the edge of the cell is so large compared to the molecule, we can assume the matrix element of the crystal Hamiltonian and the overlap matrix to be zero for any pair of basis functions not in the same cell.

$$\langle m',\mathbf{R}'|H|m,\mathbf{R}\rangle = E_m\,\delta_{m,m'}\,\delta_{\mathbf{R},\mathbf{R}'} \tag{5.5}$$

$$\langle m',\mathbf{R}'|m,\mathbf{R}\rangle = \delta_{m,m'}\,\delta_{\mathbf{R},\mathbf{R}'} \tag{5.6}$$

It follows that the band dispersion around each original molecular eigenvalue is negligible (or zero), and the eigenvectors labeled by the same n but different **k** will only differ by a phase factor, in accordance with Eq.(5.2). It is, therefore, clear that if a molecule interacts with a periodic surface in the limit of physisorption (i.e. no band

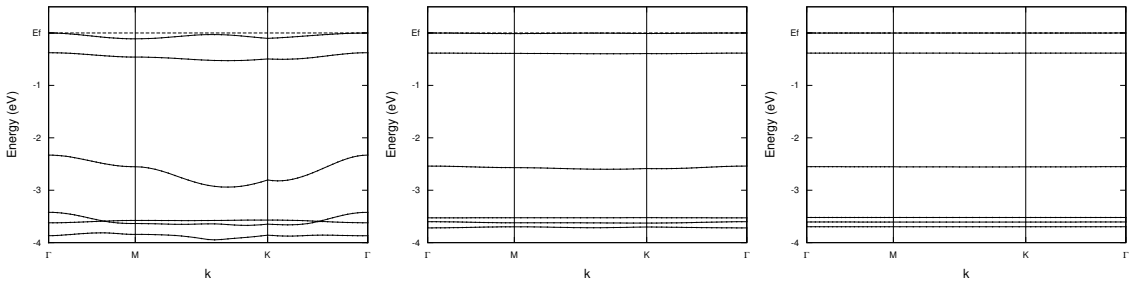

Figure 5.1: Band structure of an isolated C_4H_4S molecule in an increasingly larger simulation box (multiples of a MoS_2 surface unit). **(a)** 2×2. **(b)** 2.5×2.5 **(c)** 3×3.

mixing), and if the surface slab used is extended enough, there is no need to sample the FBZ for the molecular bands. Figure 5.1 depicts the bands of thiophene molecule in a periodic cell of different dimensions – in the largest of the three cells, the band structure is almost perfectly flat.

When researchers started simulating materials more complex than a crystal bulk, a new problem arose. I.e. the systems could include supercells with defects, stacked slabs with molecular adsorbates, and as is often the case in catalysis and photovoltaics, stacked layers of insulators and conductors. For such systems, it is not clear anymore what the ideal **k** point grid would be. The global system might be composed of parts with very different electronic structure, that in principle would require finer or coarser **k** point grids to achieve the target accuracy.

Generally a conservative choice of the **k** point sampling, i.e. choosing the one that matches the part of the system with the most complex band structure, is adopted. While this choice should preserve the quality of the predicted properties, it has the downfall of dramatically reducing computational efficiency and with that, the sizes of systems one can approach.

5.1 Method

As shown in Eq. 2.10, the density of each fragment is obtained by solving a coupled set of Kohn–Sham equations where in the embedding potential $V^I_{\text{emb}}(\mathbf{r})$ is included the interaction of the fragment I with all the other fragments.

In V^I_{emb} these interactions only depend on electron densities, and no memory about the underlying k-point sampling of the FBZ is inherited. This means that one can have total freedom in the choice of the k-point sampling of each subsystem, since the method does not require them to be all the same. If the appropriate decisions are made, this could lead to massive savings in computational time, while still retaining accuracy with respect to the full sampling reference.

In previous KS-DFT studies[59,86] it has been observed that when chemisorption of a molecule on a metal surface occurs, the localized orbitals of the molecule start hybridizing with the extended states of the metal. Analysis of the spatial distribution of the resulting Bloch states shows a sort of ghosting effect: selected molecular orbitals involved in the molecule–metal bond now exhibit partial metallic character, but at the same time metal derived bands have now contributions from those very same molecular orbitals. This effect can be expected from the fact that canonical KS orbitals are required to be orthogonal so that the kinetic energy operator is diagonal (additive), and since in KS-DFT the electronic structure of the adsorbed molecule itself becomes metallic in nature, sampling of the FBZ becomes a necessity. However, in Subsystem DFT orthogonality between orbitals of different subsystems is not imposed because each subsystem is mapped onto an independent auxiliary KS system. In place of orthogonality, the non-additive kinetic energy functional is employed. Thus, while such interactions as those arising between molecules and metal surfaces are in principle accounted for in Subsystem DFT, we can still expect the orbitals of

the molecule to be localized in space. Similar arguments can be made for computation of such observables as the dipole moment[84] – for molecular subsystems, formulas from the modern theory of polarization[112] yield equivalent results to the expectation value of the dipole operator. For these reasons, and similarly to the case of isolated molecules, the electronic structure molecular subsystems can safely be calculated at the Γ point.

5.2 Computational Details

All calculations have been performed using our in-house version of Quantum Espresso[44] – eQE – which is capable of performing Subsystem DFT simulations on periodic systems.[39,40]

For the first test system reported in this work, Ultrasoft Pseudopotentials[126] have been employed, while the PW cutoff in the expansion of the wavefunctions and electron densities is 40 Ry and 400 Ry respectively. For the second system presented, we have used Normconserving Pseudopotentials and a 90 Ry cutoff. For both systems the density functional chosen for the exchange–correlation energy is PBE.[105] The non-additive kinetic energy functional employed in the first test system is revAPBEK,[77] while for the second one LC94 (PW91k)[80] is used.

5.3 Results

For each calculation we computed not only the change in energy $\Delta E = E_{\text{calc}} - E_{\text{ref}}$, but also the number of displaced electrons $\langle \Delta\rho \rangle$, a quantity that gives an immediate

idea of how similar two electronic structures are:

$$\langle \Delta\rho \rangle = \frac{1}{2} \int |\rho_{\mathrm{calc}}(\mathbf{r}) - \rho_{\mathrm{ref}}(\mathbf{r})| \; d\mathbf{r} \tag{5.7}$$

It is also interesting to estimate how much computational throughput can be gained thanks to this local sampling of the FBZ.

Often the cpu time is dominated by the solution of the eigenvector/eigenvalue problem. Iterative diagonalization methods such as Davidson[26] are commonly employed in condensed matter in order to solve the eigenvector problem only for a selected subset of roots n_{roots}. The complexity of the Davidson algorithm is proportional to $n_{\mathrm{roots}}\, n_{\mathrm{PW}}^2$,[27] where n_{PW} is the number of plane-wave basis functions employed in the expansion of the KS orbitals, and the number of roots n_{roots} is the product of the number of bands n_{band} and the number of **k**-points n_k used to sample the FBZ.

In our original implementation,[40] all fragments shared the same simulation cell [i.e., equivalent to the common supermolecular basis set method, FDE(s)[62]]. Thus, each fragment featured the same n_{PW}. After a recent refactorization of the code (which will be presented in a separate publication) we are now able to assign fragment-specific simulation cells (smaller or equal to the supersystem cell), hence effectively providing a fragment specific PW basis set for the solution of the KS orbitals. This is the plane wave equivalent to carrying out FDE in a monomer-based basis set, termed FDE(m).[62] As n_{PW} is proportional to the volume of the simulation cell, similarly to FDE(m) this approach reduces the numerical complexity of the KS problem of each fragment.

The workload needed to obtain the eigenvalues and eigenvectors at each self-consistent field (SCF) cycle is dominated by the computation of the relevant matrices,

and it formally scales as:[27]

$$\text{Workload} \propto \sum_{I}^{N_S} n_k^I \, n_{\text{band}}^I \, (n_{\text{PW}}^I)^2 \tag{5.8}$$

The first supersystem considered is a water bilayer (12 water molecules in the simulation cell) adsorbed on a Pt surface, where each water is a fragment and so is the surface. We already performed a comparison between Subsystem DFT and KS for this system,[40] here we'll restrict ourselves to analyzing the effect of using a fragment specific sampling of the FBZ. In the reference calculation for all the fragments a $2 \times 2 \times 1$ grid is employed, while in the new calculation all the water molecules are treated at the Γ point and the metal surface retains the original sampling. As expected, the two calculations yield nearly identical results: the difference in the total energy of the supersystem is only 0.124 kcal/mol, while the number of displaced electrons is 2.6×10^{-3}.

The second test case is a challenging supersystem made of three fragments: a α-alumina surface acting as a support, a monolayer of MoS_2 on top of it, and finally a thiophene molecule adsorbed on the MoS_2. We have chosen a 2×2 supercell with respect to the α-alumina, and 3×3 with respect to the MoS_2: this allows for lattice constants of the two materials to align, and also provides enough surface to minimize the interaction of the adsorbed molecule with its periodic images. The distance between the two surfaces as well as the distance between the MoS_2 and the thiophene is set to 3.5 Å, see Figure 5.2.

This system is interesting as a test case, because given the different nature of the three fragments, we are able to span within the same supersystem many different types of electronic structures: we have a insulator (the α-alumina surface), a semiconductor (the MoS_2 film), and a gaseous molecule (the C_4H_4S).

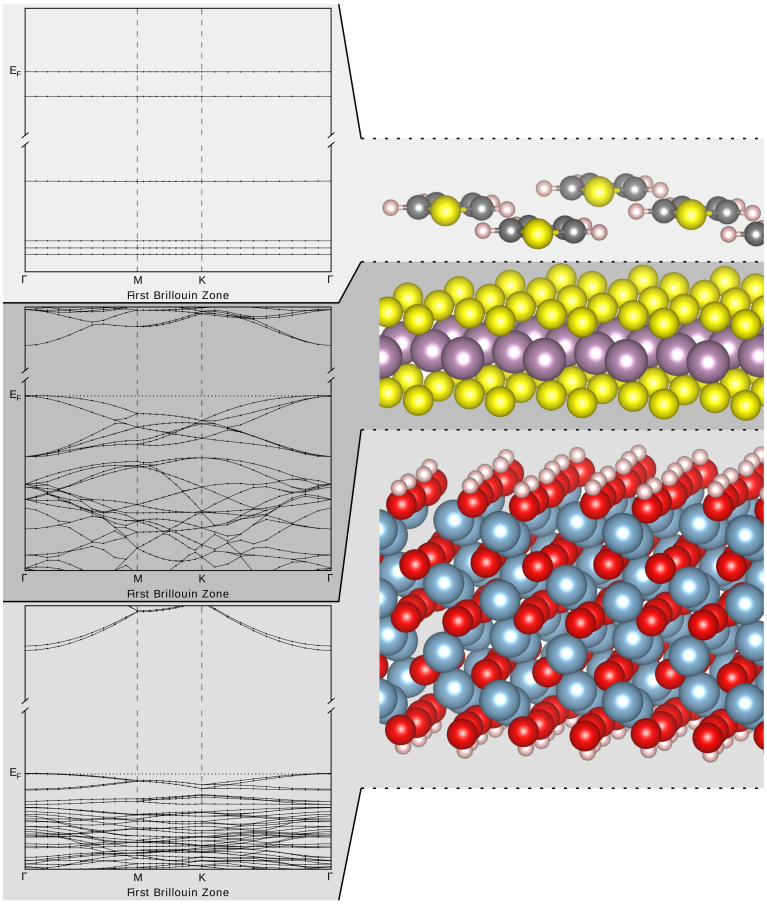

Figure 5.2: The system employed in the pilot calculation: C_4H_4S adsorbed on a MoS_2 thin film deposited on a α-Al_2O_3 slab. The band structure of the isolated fragments making the supersystem is shown to the left.

In Figure 5.2 is reported the band structure of the three isolated fragments. It should be kept in mind that the energy scale on the y axis is the same for all the three plots. As one would expect (and as we already showed in section 5.1, Figure 5.1) the band structure of the isolated molecule is perfectly flat. The band structure of the α-alumina support appears very dense from the fact that this is a 2×2 supercell, but at the same time it is relatively insensitive with respect to $\mathbf{k}$, yielding variations in the order of the tenths of eV at most. Finally the band structure of the MoS_2 film is also shown in Figure 5.2: it is clear that for this fragment a good sampling of the FBZ is particularly crucial.

In the reference calculation, a $8 \times 8 \times 1$ Monkhorst-Pack **k**-point grid has been employed in the calculation of the electronic structure of each fragment. We then systematically proceeded to calculate the same system, at the gamma point level for the molecule, and making all possible combinations in the **k**-point grids for the other two fragments: $8 \times 8 \times 1$, $4 \times 4 \times 1$, $2 \times 2 \times 1$, $1 \times 1 \times 1$.

The comparison between these 16 calculations and the reference calculation are reported in Figures 5.3a and 5.3b. From the results in the top right square we can observe that as expected calculating the thiophene fragment at the gamma point while keeping the full $8 \times 8 \times 1$ grid for the support and the thin film, introduces a negligible error: the ΔE is in the order of the 10^{-2} kcal/mol, while the displaced electrons are only 3×10^{-3} out of 668. We can also see that there is no further degradation in the quality of the results if we decrease the **k**-point grid of the alumina or the MoS_2, or both at the same time, to $4 \times 4 \times 1$. Further decreasing the grid of the MoS_2 film to $2 \times 2 \times 1$ causes a degradation in the results, no matter what grid is chosen for the alumina. ΔE is 1.5×10^{-1} kcal/mol, and $\langle \Delta\rho \rangle$ around 1.5×10^{-2}. Sampling the entire FBZ of the MoS_2 with a single **k**-point (bottom row in the chart), has the quality of the results to degrade by an additional order of magnitude.

For the α-alumina on the other hand we observe that the **k**-point grid can be safely reduced all the way down to $2 \times 2 \times 1$ without causing a significant error. It's only when the grid is reduced down to $1 \times 1 \times 1$ that we observe higher ΔE and $\langle \Delta\rho \rangle$, even though the error is not as dramatic as if the Γ-point-only grid was used for the MoS_2. All these observations are consistent with the qualitative considerations we made earlier by just observing the band structures of the isolated fragments.

Clearly, finding the right combinations of **k** point grids to be used is a system dependent problem. For this particular supersystem we show that the accuracy of the results is not affected by the choice of the FBZ sampling provided that the grids

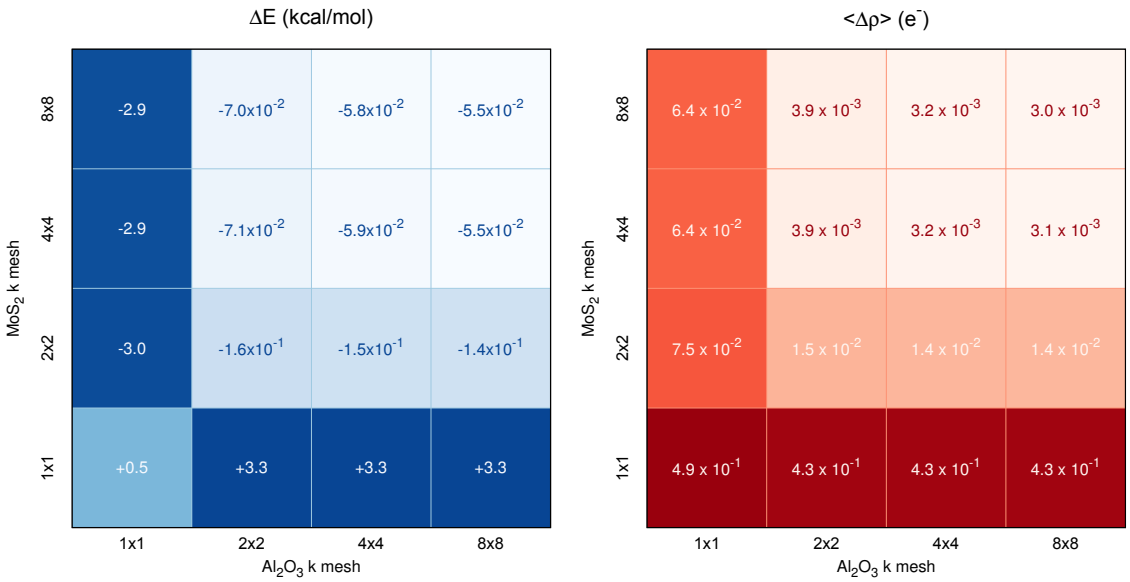

Figure 5.3: (a) Energy deviation in kcal/mol with respect to the FDE (subsystem DFT) reference calculation which was carried out employing a $8 \times 8 \times 1$ **k**-point grid for each subsystem. (b) Number of displaced electrons with respect to the reference calculation.

are not smaller than $2 \times 2 \times 1$ for alumina, and $4 \times 4 \times 1$ for MoS_2.

Now that we established that for this particular system no **k** point grid larger than $4 \times 4 \times 1$ is needed, we can proceed to compare CPU times across different methods. We will restrict ourselves to compare KS timings to four different Subsystem DFT flavors, which are Subsystem DFT with or without fragment specific simulation cells, and with or without fragment specific **k** point grids.

Table 5.1: Timings and Speedups of Subsystem DFT (SSDFT) compared to a KS reference calculation for the C_4H_4S on MoS_2 on Al_2O_3 system. # of Cycles refers to the number of SCF iterations needed to reach convergence. **(a)** Same simulation cell and **k** grid for all the fragments. **(b)** Same simulation cell but fragment specific **k** grid. **(c)** Fragment specific simulation cell but same **k** grid. **(d)** Both the simulation cells and the **k** grids are fragment specific.

	KS	**SSDFT**^{a}	**SSDFT**^{b}	**SSDFT**^{c}	**SSDFT**^{d}
Theor. Speedup	1.0×	1.0×	2.4×	5.1×	16.6×
Real Speedup	1.0×	0.9×	1.8×	1.7×	6.2×
Time / Cycle (s)	195	220	108	113	31
# of Cycles	17	88	47	23	24

In Table 5.1 theoretical speedups for each SCF cycle calculated according to Eq. 5.8 are reported, as well as actual CPU times obtained by running the simulation in parallel over 80 processors. The number of processors assigned to each fragment varies in each calculation, in order to obtain the best distribution of the workload and minimize idle time. From these results we observe that for this particular system the full potential of Subsystem DFT is only unlocked when both the **k** point grid and the simulation cell are fragment specific, yielding in the best case up to a six-fold real speedup over a reference KS calculation with no loss in the quality of the calculation other than the error introduced by employing Subsystem DFT itself. Notable is also the fact that reducing the simulation cell of the fragments has the positive effect of causing the SCF procedure to require fewer steps to reach convergence, thus decreasing the total wall time of the simulation. We attribute this to a reduced amount of vacuum in the expansion of the subsystem orbitals.

5.4 Conclusions

Computational complexity of materials modeling is given by two factors. One is the number of electronic levels that needs to be computed, $n_k \cdot n_{\text{band}}$. The other is given by the square of the basis set size (e.g. plane waves), n_{PW}^2. In this work, we have focused on reducing the former by devising a local sampling of the first Brillouin zone. This was possible because of a subsystem DFT description of the electronic structure of the system.

We recognize, however, that to achieve breakthrough speedups, also the basis set size needs to be tailored to the single subsystems.

Chapter 6

Ab Initio Molecular Dynamics

This chapter is adapted from the following peer-reviewed paper:

- Alessandro Genova, Davide Ceresoli, and Michele Pavanello. Avoiding Fractional Electrons in Subsystem DFT Based Ab-Initio Molecular Dynamics Yields Accurate Models For Liquid Water and Solvated OH Radical. *J. Chem. Phys.*, 144:234105, 2016

The ability of the FDE to provide an improved description over KS-DFT of liquids and solvated radical species is explored in this chapter. The liquids are studied here by Ab-Initio Molecular Dynamics (AIMD) with forces computed on-the-fly by the FDE method.

There is little doubt that the Kohn–Sham formulation of Density Functional Theory[71] (KS-DFT) is the most popular and promising all-electron electronic structure method there is. Because explicit analytical forms of the exact density functional

are unknown, practical implementations of KS-DFT necessitate approximations at the level of the exchange and the correlation energy functionals. The approximations most often invoked are the local density approximation[129] (LDA) and the generalized gradient approximation[9,103] (GGA) which assume the energy functional to be dependent only on the value of the electron density, $\rho(\mathbf{r})$, and its gradient, respectively, at all points in space $\mathbf{r} \in \mathbb{R}^3$. So-called hybrid functionals (which mix Hartree-Fock exchange with GGA exchange) are also plentiful in the literature, even though they involve departing from the KS-DFT framework and embracing the generalized KS-DFT scheme.[106,116]

Because evaluating the electron density requires a number of operation that grows linearly with system size, and evaluation of the density gradient requires at most $N \log(N)$ operations with N being the number of grid points used in the discretization of space (similar complexities arise when atom-centered basis functions are employed in place of discretization of space), LDA and GGA result in computationally amenable algorithms.

The drawback of employing these approximations is twofold: complete neglection of electron correlation effects that arise at long ranges[76] (e.g. van der Waals interactions), and the unfortunate side effect that due to the approximate nature of the exchange functional, electrons nonphysically partially interact with themselves. That is, they self-interact.[104]

Self-interaction error (SIE) has been termed *an outstanding failure*[18] of KS-DFT. This error poses serious challenges as it has the effect of overdelocalizing electrons,[24] especially in molecules containing unpaired electrons.[128] When metal surfaces are involved, the reactive scattering experiments, such as the ones involving diatomics, in recent years have puzzled researchers [most notably O_2+Al(111)] because of the complexity introduced by the SIE.[11,19,81–83] When radical species are involved, SIE

overdelocalizes the spin-density.[25,85,137] An example is $OH^{\bullet}$ radical in water,[127,128] and radical cations of biological systems.[67,101,118]

The delocalization of the spin density is related to the fact that in the presence of self-interaction, electrons prefer to be spread over multiple sites with a fractional electronic occupation on each site. This is known as the problem of "fractional charges",[24] and when there are unpaired electrons, for the same reason delocalization is witnessed also for the spin density. Unfortunately, a universal and computationally amenable solution to this problem is still to be found.[18] The use of hybrid functionals partially corrects for the SIE, and so does the use of model potentials with corrected long-range behavior.[20,21,23,52,54,115,122]

Similarly to constrained DFT,[138] fragment-based DFT and wavefunction approaches, such as subsystem DFT,[62,73,136] and the Fragment Molecular Orbital method,[48] have shown ability to constrain the spin density of radicals in a spatially localized region of space spanned by a single subsystem (or fragment).[67,97,98,101,118] Such a localization is in part due to the use of monomer-only basis sets, and also due to other features of the method which in effect apply constraints to the spatial extension of the electron density of each fragment.[95,102,108,110] The method has the beneficial effect of not allowing charges to delocalize, thus effectively generating diabatic states, and generally leading to more physical electron spin densities.[101,118]

The drawback associated to such fragment-based approaches is that the investigator needs to already know the underlying physics of the system in order to know where and to what extent the spin density needs to be localized. This argument, however, can be (at least partially) fended off by noticing that it is possible to generate several spin (or charge) localized states for the studied system, and then compute the electronic coupling between them.[102,109,119] This would be a way of determining if the localized state is a physical state (i.e. when such a coupling is small) rather

than just a localized diabatic state.

6.1 Energy gradients with respect to nuclear coordinate displacements

Nuclear gradients for the FDE method have been first presented by the Wesolowski group,[30,132] and later by Iannuzzi *et al.*[61] Recently, the quest for accurate and computationally efficient evaluation of gradients also for excited electronic states led to additional work by the Neugebauer group.[72]

We have developed FDE energy gradients building on the already available gradients in the Quantum-Espresso package.[44] These involve the evaluation of Hellmann–Feynman gradients of the electron–nuclear attraction term, of the nuclear–nuclear repulsion terms evaluated through Ewald-type summations, and for ultrasoft (US) and projector augmented wave (PAW) pseudopotentials evaluation of Pulay-like terms is needed.[89]

Our contribution was limited to the introduction of the nonadditive energy functionals for which we can now compute the core density contributions. These are computed analytically following the recipe found in section 4.5 of Ref.89.

The XC and the non-additive kinetic energy (and potentials) are generally evaluated for a density that includes not only the bare valence electron density ρ, but it may also includes a smooth core density $\tilde{\rho}_{\text{core}}$:

$$E_{\text{XC}} = E_{\text{XC}}[\rho + \tilde{\rho}_{\text{core}}] \tag{6.1}$$

Generally, the smooth core density is provided by the pseudo potential in the form of a spherical Bessel function centered in the origin $\tilde{\rho}^{A}_{\text{core}}$, and the total core density

of the system is the sum of the core densities of each atom appropriately translated:

$$\tilde{\rho}_{\text{core}}(\mathbf{G}) = \sum_A \tilde{\rho}^A_{\text{core}}(\mathbf{G})\, S_A(\mathbf{G}) \tag{6.2}$$

where $S_A(\mathbf{G}) = e^{-i\mathbf{G}\cdot\mathbf{R}_A}$ is the structure factor.

Since the core density depends explicitly on the position of the atoms, it leads to a new contribution to the forces acting on the nuclei:

$$f^A_{\text{nlcc}} = -\Omega \sum_{\mathbf{G}} i\mathbf{G}\, v(\mathbf{G})\, \tilde{\rho}^A_{\text{core}}(\mathbf{G})\, S_A(\mathbf{G}) \tag{6.3}$$

where v includes the exchange-correlation potential, as well as the non-additive potentials.

6.2 Computational details

We have considered two condensed-phase systems: liquid water and solvated $OH^\bullet$ radical.

- water64: 64 water molecules (64 subsystems) in a cubic periodic box of lattice vector $a = 12.43$Å. The AIMDs featured 81,000 steps with a timestep of 26 a.u. (1 a.u. $= 2.418884 \times 10^{-17}$ s). The first 25,000 steps were discarded. The remaining steps were used to generate the results. KS-DFT results were obtained from a 64,000-step AIMD discarding the first 25,000.

- water256: 256 water molecules (256 subsystems) in a cubic periodic box of lattice vector $a = 19.73$Å. 34,000 steps with a timestep of 26 a.u. The first 16,000 were discarded.

- The solvated $OH^\bullet$ system was generated from the water64 system by removing

one H atom from one water molecule. FDE results were extracted from a 33,000-step dynamics, again using a 26 a.u. time step. The first 12,000 steps were discarded.

All calculations were run at the Γ-point. When we used US pseudopotentials (pbe-rrkjus.UPF from the main Quantum-Espresso pseudopotential library for the water simulations, and the GBRV[38] for the $OH^{\bullet}$ simulations), 40Ry and 400Ry are the energy cutoffs for the plane wave expansions of the molecular orbitals and the charge density, respectively. We also employed NC pseudopotentials for the water simulations (O.pbe-mt_fhi.UPF and O.pbe-mt_fhi.UPF converted from the *abinit* pseudopotential library), we used cutoffs of 100Ry and 400Ry for the waves and the density, respectively. The periodic box used for the plane wave expansion of each subsystem was customized to have a lattice vector which is 60% of that of the native box for water64 and 40% for water256. This allowed us to reduce the number of plane waves for each water molecule from 55×10^3 to 12×10^3, for water64 and from 221×10^3 to 14×10^3 for water256. A description of the setup is depicted in Figure 3.2a. Hartree potentials and nonadditive potentials were computed on the native grid redefining the message passing interface (MPI) communicator to use all available processors.[39] We use 4 processors per water molecule, totalling 256 processors for water64, and 8 processors for $OH^{\bullet}$. In water256, we used one processor per water molecule.

The $OH^{\bullet}$ simulations were run imposing a total magnetization (i.e. integral of the spin density) to be equal to unity. In addition, the $OH^{\bullet}$ subsystem was embedded in 63 closed-shell water molecules. We have chosen this set up exclusively to speed up the simulations, as preliminary test computations allowing all the water molecules to be spin polarized, did not induce any appreciable or significant spin polarization in the water molecules.

In all AIMD simulations, temperature was kept at 340K ± 30K using velocity rescaling, and the dynamics was driven by the Verlet algorithm.

6.3 Results

6.3.1 Liquid water

Liquid water has been the test bed for DFT and quasiparticle methods for decades now. The main drawback of semilocal KS-DFT in the simulation of this liquid is that it fails in reproducing the liquid state, favoring instead a sort of glassy, solid state at standard temperature and pressure (see section 9.5 of Ref. 89 as well as recent publications[28,36]). It has recently been shown that the inclusion of 25% of Hartree–Fock exchange in the functional (using PBE0) and the inclusion of van der Waals forces in the functional delivers an accurate description.[28,36] The reasons for the failure of LDA and GGA functionals can be largely ascribed to the self-interaction error. For example, it is known that semilocal KS-DFT overestimates the fraction of charge-transfer character in the hydrogen bond.[68,69] This has the effect of making the hydrogen bond too strong, too directional which in turn makes liquid water too sluggish (most accurate diffusion coefficient from PBE is $0.789 \times 10^{-5}\,\mathrm{cm^2 s^{-1}}$ from Ref. 74 against the experimental $2.34 \times 10^{-5}\,\mathrm{cm^2 s^{-1}}$).

Subsystem DFT (in various flavors) has been applied to liquid water providing us with a surprisingly diverse set of conclusions on its ability to deliver acceptable models. The first simulation is due to Barker and Sprik,[7] which showed that using frozen-density water molecules artificially augmented by a *ad hoc* dipole moment, delivered quantitative agreement with the experiment. Later, Iannuzzi *et al.*[61] applied fully selfconsistent FDE to water64 using various nonadditive kinetic energy

functionals (both LDA and GGA) and concluded that the kinetic energy functionals available at the time were not accurate enough to produce a structured water – all their simulations yielded a nonstructured liquid with an absent second solvation shell.

Later, Hodak *et al.*[58] showed that once again quantitative agreement with experiment can be obtained by allowing KS-DFT to describe only water molecules in the first solvation shell while from the second solvation shell onward, frozen-density water molecules were simulated in a way similar to Barker and Sprik.[7]

The state-of-the-art of subsystem DFT methods applied to liquid water is therefore confusing: if the water molecule's density is treated selfconsistently according to FDE, the liquid is nonstructured. If, instead the molecular density is kept fixed and electrostatics is treated semiempirically, the models yield a more physical picture.

Because it is difficult to pinpoint the exact reasons for this behavior, rather than embarking ourselves into complex analysis of other group's work, we instead carried out our own simulation of liquid water. We first started by analyzing the water dimer. This time, not only against semilocal KS-DFT but also against very accurate Potential Energy Surface (PES) computed at the CCSD(T) level of theory.[4] We collect our analysis in Figure 6.1.

From Figure 6.1, we notice two general behaviors: (1) The LC94[80] and the revAPBEK[77] nonadditive kinetic energy functionals behave very similarly to each other with the revAPBEK being a little more repulsive as a function of angles [see insets (c) and (d)], and a little more attractive as a function of the oxygen–oxygen distance [see inset (b)]; (2) For the angular PES cuts, the CCSD(T) benchmark is positioned in between KS-DFT and the FDE results obtained with LC94 and revAPBEK. The TF functional[34] instead does not behave neither quantitatively nor qualitatively correctly for this system.

Our results comparing KS-DFT with FDE are in perfect agreement with previous

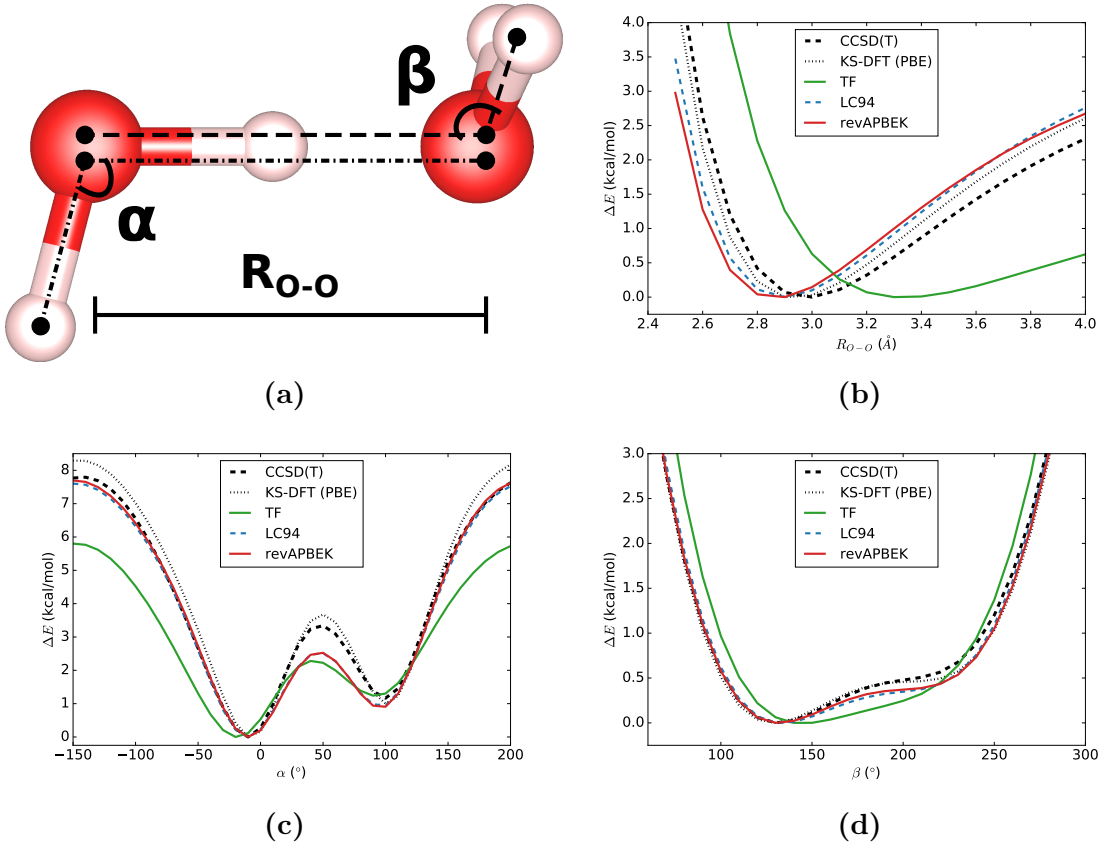

Figure 6.1: (a) The definition of R_{O-O} and the α and β angles. PES cuts: (b) at frozen $\alpha = 104$ and $\beta = 70$ along R_{O-O}, (c) at frozen $\beta = 70$ and $R_{O-O} = 2.9$ along α, (d) at frozen $\alpha = 104$ and $R_{O-O} = 2.9\AA$ along β. The labels are as follows: Thomas–Fermi (TF),[34] Lembarki–Chermette (LC94),[80] and revised APBEK (revAPBEK)[77] nonadditive kinetic energy functionals employed in the FDE simulations. Both KS-DFT and FDE simulations employed the PBE xc functional.

studies.[61,130] From the results of the dimer, we could predict that FDE should yield structured liquid water, softer than semilocal KS-DFT with a hydrogen bond distance that is slightly shorter (by about 0.1 Å).

Results of our water AIMD are presented in Figure 6.2. They follow exactly the trends experienced by the dimer. That is, the LC94 water is generally softer than revAPBEK's, and semilocal KS-DFT is too structured. The results for the LC94 functional partially disagree with Iannuzzi *et al.*[61] in the fact that LC94 retains a second solvation shell well after 10ps of dynamics. However, we point out that

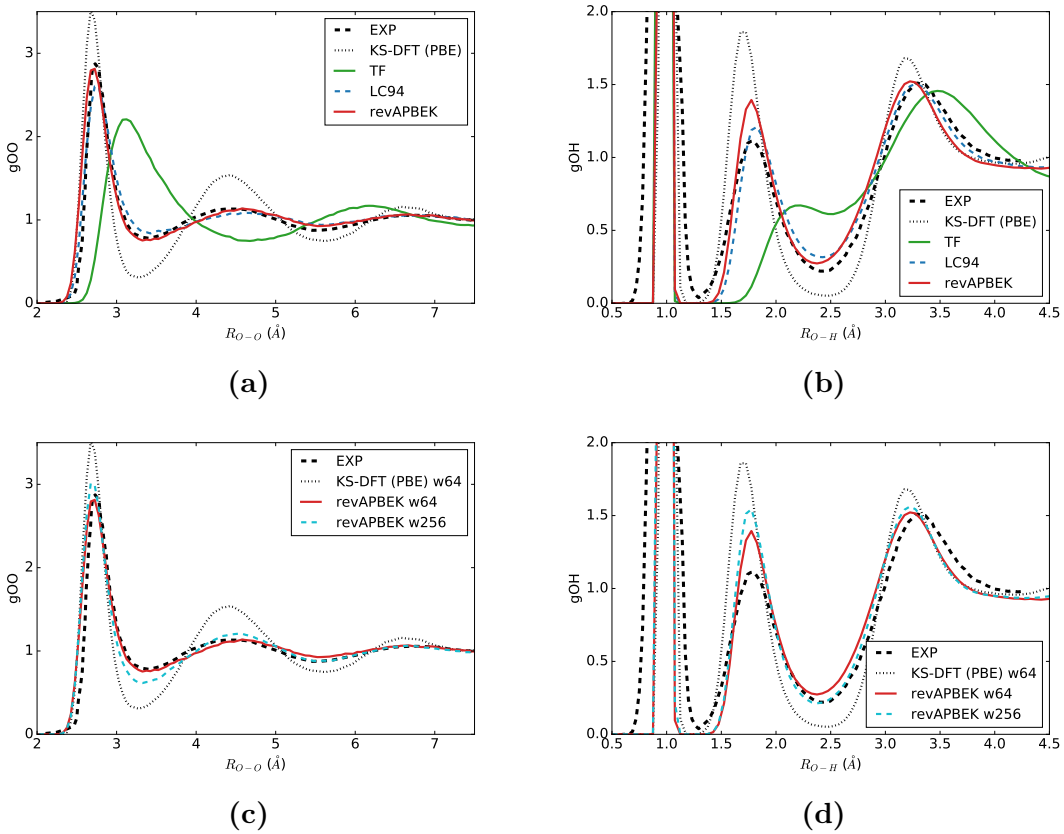

Figure 6.2: Radial distribution functions obtained with different nonadditive kinetic energy functionals. The labels are defined in Figure 6.1, EXP is the experimental value.[60,117,120,121] (a) Oxygen–oxygen for water64, (b) oxygen–hydrogen for water64, (c) Oxygen–oxygen for water256, (d) oxygen–hydrogen for water256. KS-DFT results are for water64.

among the GGA functionals that we used, LC94 delivers the softest (least structured) water. Thus, we propose to use revAPBEK in future FDE simulations of this system. TF results are unphysical as expected from the poor dimer PES cuts. Our results are internally coherent and fairly independent of the pseudopotential used. In the supplementary information section,[32] we provide the reader with radial distribution plots obtained with NC pseudopotentials. Although they are not quantitatively equal to the ones presented in Figure 6.2, the overall trends remain. The variability between different types of pseudopotentials is expected and already documented for KS-DFT (see for example Ref. 79).

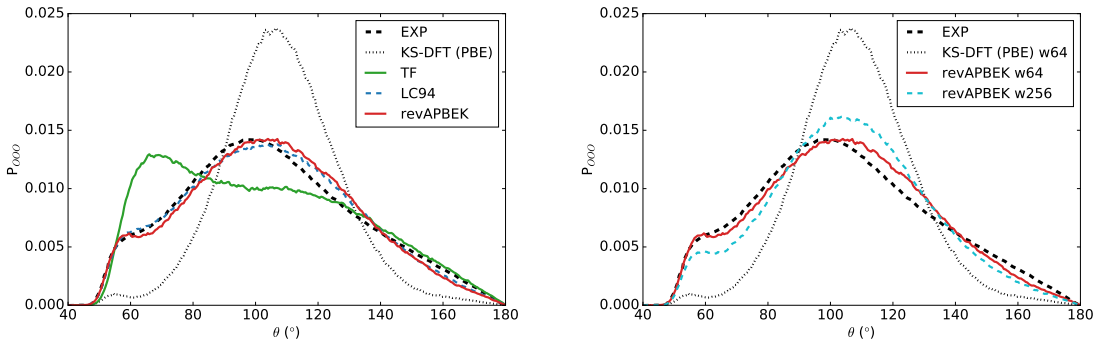

(a) **(b)**

Figure 6.3: Oxygen-oxygen-oxygen angular distributions for water molecules within the same solvation shell (3.7Å cutoff). The experimental distribution is taken from Ref. 120. Inset (a) compares various nonadditive kinetic energy functionals. Inset (b) compares water64 with water256.

In inset (d) of Figure 6.2, we report comparisons between the results obtained for water64 and the ones for water256. We are aware that to make a meaningful comparison between these two systems, we should run longer dynamics (e.g. the order of 250ps long[74]). However, we see that also water256 features a structured water with a second solvation shell. We note that we do expect differences between water256 and water64 as the former is already close to the thermodynamical limit in which the NVE ensemble becomes equivalent to the NVT ensemble. In fact, we notice that no velocity rescaling events took place in the 11ps long production run for water256. Thus, in theory water64 and water256 reflect two different thermodynamical ensembles and as a result should differ in their dynamical behavior.

In Figure 6.3 we report the oxygen-oxygen-oxygen angular distributions for water molecules within the same solvation shell. Once again, and in agreement with other studies,[28] the KS-DFT employing PBE is found to be too structured with a too large probability of finding water molecules in a tetrahedral distribution ($\theta \simeq 109^o$). The FDE results provide semiquantitative agreement with the experiment and maintain the already mentioned trend having TF delivering unphysical results, and with LC94

Table 6.1: Computed diffusion coefficients (D) and their standard deviation (σ_D) for the FDE and semilocal KS-DFT (employing the PBE xc functional) simulations compared with the experimental value. Units are $10^{-5}\,cm^2s^{-1}$.

	D	σ_D
EXP	**2.34**	
KS-DFT (PBE)	0.43	0.07
TF	6.81	0.37
LC94	4.76	0.42
revAPBEK	2.97	0.42
revAPBEK (w256)	3.54	0.23

yielding a slightly softer water than the revAPBEK kinetic energy functional. Results for the water256 system show again a slight overstructuring compared to water64. Results from NC presudopotentials are reported in the supplementary materials.[32]

We also computed the diffusion coefficient of the liquid and found good agreement with the experimental value, see Table 6.1. Specifically, we notice that the TF non-additive functional is too soft and allows water to diffuse too much. Between LC94 and revAPBEK, it is revAPBEK that delivers the best agreement. Results for water256 are in fair agreement to the ones for water64, considering that the simulations were run for only 52ps for water64 and 22ps for water256. As our AIMD simulations are relatively short, we have a fairly large uncertainty on the reported diffusion coefficients.

6.3.2 Solvated $OH^\bullet$ radical

DFT simulations of $OH^\bullet$ also have an interesting history. It all started with a simulation by Vassilev *et al.*[128] showing that the $OH^\bullet$ has the capability of forming a quasi-covalent bond with nearby water molecules (hemibonds). The spin density in Ref. 128 was delocalized between the $OH^\bullet$ and several surrounding water molecules. This behavior is unfortunately not supported by experiments,[15] nor by self-interaction

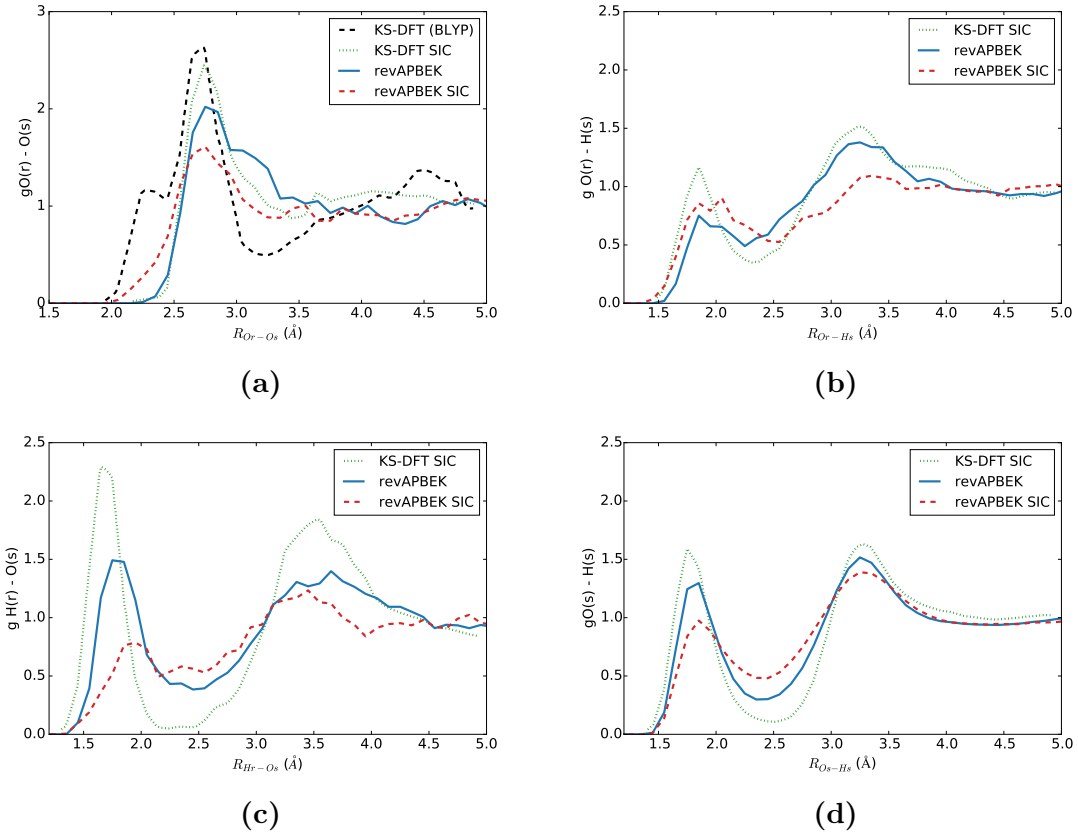

Figure 6.4: Radial distribution functions of the $OH^{\bullet}(H_2O)_{63}$ system. (a) Oxygen(radical)–oxygen(solvent), (b) oxygen(radical)–hydrogen(solvent), (c) hydrogen(radical)–oxygen(solvent), (d) oxygen(solvent)–hydrogen(solvent). revAPBEK stands for pure FDE simulations, while revAPBEK SIC is a FDE simulation in which the $OH^{\bullet}$ subsystem has been treated with the self-interaction correction proposed by VandeVondele and Sprik in Ref. 127 (from which the KS-DFT and KS-DFT SIC reference curves obtained with the BLYP functional are also taken).

corrected KS-DFT simulations.[127]

Having built confidence from the results for liquid water, and knowing that the radical in the $OH^{\bullet}$ should be localized on to the OH fragment, we set out to simulate AIMD of $OH^{\bullet}$ solvated by 63 water molecules. Results of our simulations are summarized in Figure 6.4.

As the subsystem's electron densities are constrained to integrate to a whole number of electrons, the fractional electron problem typical of semilocal GGA xc functionals has no chance of appearing. This is reflected in the results, as we see from

inset (a) of Figure 6.4, the first solvation shell occurs at 2.7Å in agreement with Ref. 127. Inset (b) and (c) show that the hydrogen bonds between the water molecules and the radical are not particularly strong compared to those in the bulk of the solvent shown in inset (d). Once again, this agrees well with self-interaction corrected KS-DFT simulation and depart from the idea of the formation of the hemibond proposed before.[128] When we apply the self-interaction correction proposed by VandeVondele and Sprik in Ref. 127 to the $OH^{\bullet}$ subsystem, we generally do not improve the results. This signifies that the pure FDE AIMD simulations already provide a physical picture of the dynamics of solvated $OH^{\bullet}$.

6.4 Conclusions

In conclusion, we have explored the possibility of ridding AIMD simulations of the self-interaction error by exploiting a subsystem DFT description of the electronic structure. By expanding the total electron density in terms of localized subsystem electron densities that are constrained to integrate to a preset number of electrons, a system such as solvated $OH^{\bullet}$ can be successfully simulated. Besides $OH^{\bullet}$, we have shown that our subsystem DFT implementation is capable to qualitatively reproducing the dynamics of liquid water. Radial distribution functions and diffusion coefficient are in good agreement with the experiment provided that a quality nonadditive kinetic energy functional is employed.

The success of our method is due to two factors: (1) the self-interaction error due to the problem of "fractional charges" between subsystems is absent, and (2) the nonadditive functional revAPBEK is capable of reproducing the complex potential energy surface of the water dimer more accurately than any other GGA kinetic energy functional ever employed for liquid water. The combination of these two factors

provides us with a semiquantitative method for modeling aqueous environments.

Thus, we can conclude that the qualitative improvement of the subsystem DFT treatment compared to semilocal DFT for the systems considered in this work is due to the fact that the nonadditive kinetic energy functionals cancel out errors that arise from the use of semilocal GGA functionals (in our case PBE). Such a strategy has proven successful also when applied to bond dissociation. Nafziger and Wasserman showed that this error cancellation gives rise to the formation of a step in the Kohn-Sham potential of the supersystem that is completely missing in semilocal exchange–correlation potentials.[96] The step was linked to static correlation effects important to the description of bond dissociation.[17,124] We have also previously exploited the same error cancellation when we applied subsystem DFT to the computation of diabatic states for electron transfer reactions.[101,110]

Chapter 7

An attempt to address DFT Self Interaction Error

7.1 Introduction

In chapter 6 it was reported that FDE can be an effective tool to get around DFT self-interaction error and obtain physical results. This has been applied in molecular dynamics of liquid water, where self interaction leads to hydrogen bonds which are too strong, and to dynamics of the OH radical in water, where spin density leakage leads to unphysical semi-bonded states between the radical and neighboring water molecules.

FDE does so well in these instances largely due to error cancellation. The non-additive potential has been shown to have repulsive walls in the vicinity of the atoms of the environment, leading to a confinement of the electrons of the active system. On the other hand, the self-interaction error causes electrons to repulsively interact with themselves, leading to delocalization. FDE takes advantage of the delicate balance between these two opposite driving forces.

While there is quality in a tool that can effectively exploit error cancellation, from a theoretical point of view it would be an even bigger achievement to correct for the self interaction error explicitly.

Several methods have been proposed in the past to achieve this. The method proposed in 1981 by Perdew and Zunger (PZ)[104] prescribes to explicitly subtract the self interaction energy of the electrons from the total energy,

$$E_{\mathrm{XC}}^{\mathrm{SIC}} = E_{\mathrm{XC}}[\rho_\alpha, \rho_\beta] - \left(\sum_{n,\sigma} E_{\mathrm{H}}[\rho_{n\sigma}] + E_{\mathrm{XC}}[\rho_{n\sigma}, 0] \right) \tag{7.1}$$

where $\rho_{n\sigma}$ is the electron density associated with the n-th KS orbital.

While Perdew and Zunger approach does improve the description of atoms, it yields orbital specific potentials which are non-invariant to a rotation of the basis, and is of limited practical use in most systems.

A special case of the PZ correction has been proposed by VandeVondele *et. al.*[127] and can be used to correct for the self interaction of spin densities:

$$E_{\mathrm{XC}}^{\mathrm{SIC}} = E_{\mathrm{XC}}[\rho_\alpha, \rho_\beta] - (aE_{\mathrm{H}}[\rho_\alpha - \rho_\beta] + bE_{\mathrm{XC}}[\rho_\alpha - \rho_\beta, 0]) \tag{7.2}$$

Another popular approach is to add a fraction of the Hartree-Fock exact exchange to a local or semi-local exchange functional. These hybrid functionals[2,10,56,123] yield the highest accuracy, but suffer from performance issues. Since they require the evaluation of two electron integrals between all pairs of occupied KS orbitals, their cost quickly becomes prohibitive as the number of electrons increases. This is especially true for periodic systems, where the sampling of the first Brillouin zone introduces additional complexity.

A different approach to rid of self interaction is to consider the asymptotic behavior

of the exchange and Hartree potentials. For an arbitrary localized electron density of N electrons, the Hartree potential at long range is

$$\lim_{r\to\infty} V_{\mathrm{H}} = \frac{N}{r}. \tag{7.3}$$

This is intuitively unphysical, because it implies that an electron is interacting with its own density.

However, to correct this unphysical behavior it would be enough to have an exchange potential such that

$$\lim_{r\to\infty} V_{\mathrm{X}} = -\frac{1}{r} \tag{7.4}$$

In 1994 van Leeuwen and Baerends proposed a model potential (LB94) that has the desired $-\frac{1}{r}$ for exponentially decaying electron densities.[125]

The LB94 is not perfect however: since it is not the functional derivative of any density functional, it yields inaccurate energies and spurious forces. And while it has the correct long range behavior, it is inaccurate at short range.

To overcome the latter, in 1999 Gritsenko *et. al.*[51,52] proposed a potential which at each point in space would be the statistical average between a suitable $\mathrm{XC_{in}}$ potential and the LB84 potential. The weight of this average would be given according to the relative ratios between the HOMO density and the total density. The SAOP potential would then be capable to provide accurate potentials both in the short range (thanks to the contribution of $\mathrm{XC_{in}}$), as well as the long range (thanks to LB94).

Driven by the promise of an accurate model potential that can be evaluate at the same of any other GGA functional, we set off to derive an implementation that could be used in plane waves simulation packages.

7.2 Implementation

7.2.1 Regularizing the density and its gradient

For an exponentially decaying density the LB94 potential correctly goes as $-\frac{1}{r}$, and it is useful to capture this behavior for as far from the system as possible. This means dealing with areas where the electron density is extremely small. It is a known fact that expanding any function in a finite plane wave basis yields small oscillations, that also trickle down to the gradient of such functions. The combination of small densities and inaccurate gradients is a recipe for disaster when used with a numerically unstable functional such as LB94. In fact, when using plane waves LB94 yields extremely inaccurate and noisy potentials right in the areas where it is most crucial.

To find a solution, we approached the problem from two sides. We introduced an auxiliary smooth electron density $\tilde{\rho}$ evaluated as

$$\tilde{\rho}(\mathbf{r}) = \int \delta(\mathbf{r}' - \mathbf{r})\rho(\mathbf{r}')\,\mathrm{d}\mathbf{r}' \tag{7.5}$$

where δ has a finite width and effectively averages the value of ρ at a point with its neighbors. This convolution is efficiently performed in reciprocal space.

We also introduced an auxiliary smooth gradient $\nabla\tilde{\rho}$:

$$\tilde{\rho} = \sqrt{\tilde{\rho}}\sqrt{\tilde{\rho}}, \quad \rightarrow \quad \nabla\tilde{\rho} = 2\sqrt{\tilde{\rho}}\left(\nabla\sqrt{\tilde{\rho}}\right) \tag{7.6}$$

Here we take advantage of both, the fact that we evaluate the gradient of a smoothened density, and the fact that multiplying $\nabla\sqrt{\tilde{\rho}}$ by $\sqrt{\tilde{\rho}}$ should quench any artifacts when $\rho \to 0$.

Finally, the density and the gradient fed to the LB94 potential are a combination

of the original quantities and the smoothened ones.

$$\rho_{\text{final}}(\mathbf{r}) = w(\mathbf{r})\,\rho(\mathbf{r}) + [1 - w(\mathbf{r})]\;\tilde{\rho}(\mathbf{r}) \tag{7.7}$$

where

$$w(\mathbf{r}) = \begin{cases} 1, & \text{if } \ln\rho(\mathbf{r}) > h \\ \dfrac{\ln\rho(\mathbf{r}) - l}{h - l}, & \text{if } h >= \ln\rho(\mathbf{r}) > l \\ 0, & \text{if } \ln\rho(\mathbf{r}) <= l \end{cases} \tag{7.8}$$

and h, l are arbitrary parameters.

The chosen $w(\mathbf{r})$ ensures that ρ_{final} matches the original rho in those regions where the density didn't need smoothing to begin with, and that it transitions to $\tilde{\rho}$ linearly with respect to r for exponentially decaying densities.

7.2.2 Statistical average in reciprocal space

The original SAOP potential relies on the ratio between the HOMO density and the total density to determine the weight in the average between an inner potential and an outer potential (LB94).

Once again, for numerical reasons, this was not a viable option for a plane wave package.

One option would be to devise a strategy that assigns the weights solely based by the total density. However this would only work for isolated systems, while for condensed phase systems the outer potential would never get the chance to kick in.

Instead, we opted for a strategy that mixes short range and long range in reciprocal space, in the same spirit as other range separated hybrid functionals.[56]

The exchange potential can be written as

$$v_X(\mathbf{r}) = \int \frac{1}{|\mathbf{r}-\mathbf{r}'|}\,\rho_X(\mathbf{r}')\,d\mathbf{r}' \tag{7.9}$$

where

$$\rho_X(\mathbf{r}) = F^{-1}\left[\frac{|\mathbf{G}|^2}{4\pi}\,\bar{v}_X(\mathbf{G})\right] \tag{7.10}$$

The term $\frac{1}{|\mathbf{r}-\mathbf{r}'|}$ can be separated into a short range (SR) and a long range part (LR):

$$\frac{1}{|\mathbf{r}-\mathbf{r}'|} = \frac{1}{r_{12}} = \underbrace{\frac{e^{-\alpha r_{12}}}{r_{12}}}_{\text{SR}} + \underbrace{\frac{1}{r_{12}} - \frac{e^{-\alpha r_{12}}}{r_{12}}}_{\text{LR}} = \text{SR}(r_{12}) + \text{LR}(r_{12}) \tag{7.11}$$

Eq. 7.9 can be rewritten in terms of the range separation, which also gives the flexibility of using two different ρ_X, one appropriate at short range, and one appropriate at long range.

$$v_X(\mathbf{r}) = \int \text{SR}(|\mathbf{r}-\mathbf{r}'|)\,\rho_X^{\text{SR}}(\mathbf{r}') + \text{LR}(|\mathbf{r}-\mathbf{r}'|)\,\rho_X^{\text{LR}}(\mathbf{r}')\,d\mathbf{r}' \tag{7.12}$$

Eq. 7.12 can be efficiently evaluated in reciprocal space, since the Fourier transforms of both SR and LR are known analytically:

$$\text{SR}(\mathbf{G}) = \frac{4\pi}{|\mathbf{G}|^2+\alpha^2}, \quad \text{LR}(\mathbf{G}) = \frac{4\pi}{|\mathbf{G}|^2} - \frac{4\pi}{|\mathbf{G}|^2+\alpha^2} \tag{7.13}$$

Finally, combining Eq. 7.10, Eq. 7.12 and Eq. 7.13 we obtain

$$v_X(\mathbf{r}) = F^{-1}\left[\bar{v}_X^{\text{SR}}(\mathbf{G})\,\frac{|\mathbf{G}|^2}{|\mathbf{G}|^2+\alpha^2} + \bar{v}_X^{\text{LR}}(\mathbf{G})\,\left(1 - \frac{|\mathbf{G}|^2}{|\mathbf{G}|^2+\alpha^2}\right)\right] \tag{7.14}$$

LB94 is chosen for v_X^{LR}, as it has the appropriate asymptotic behavior at long range to correct the self interaction error. Other GGA exchange functionals can be

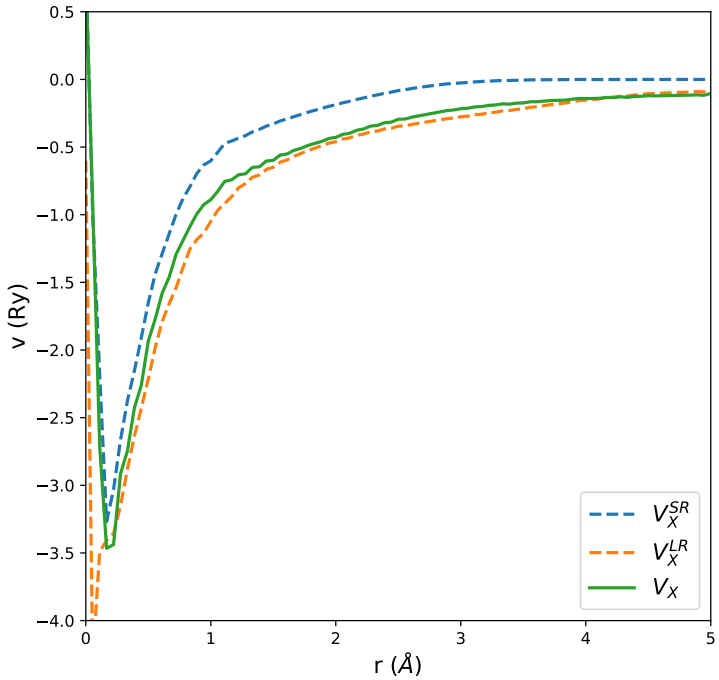

Figure 7.1: Depiction of how the model potential from Eq. 7.14 transitions from v_X^{SR} to v_X^{LR} in a Ne atom.

chosen for v_X^{SR}.

7.3 Results

A stable implementation of Eq. 7.14 has been included in Quantum Espresso. The smoothing explained in section 7.2.1 consistently yields a numerically stable LB94 potential.

The potential is stable and led all the systems it was applied on to self consistency.

The model potential derived in reciprocal space, has the the expected behavior in real space: at short range it resembles the chosen short range potential, and it smoothly switches to the long range potential at long range. An example is provided

for the Neon atom in Fig. 7.1.

The model potential is also applied to the chloride anion. The most remarkable result for this system is that the model potential yields a localized s-like LUMO, whereas the same calculation using PBE yields a completely delocalized LUMO.

Unfortunately, when applied to systems other than atoms, the model potential never provided an improvement over a regular GGA potential.

The model potential has been applied to the OH radical in water, but spin density leakage to neighboring water molecules has been observed. This is an indication that for this system the the model potential is affected by self interaction error like any other GGA functional.

Finally, the model potential has been tested on the interaction between an Al(111) slab and an oxygen molecule. In a previous study[82] it has been shown that after correcting the self-interaction error through hybrid functionals (HSE06 and PBE0), the LUMO energy of the Oxygen raises above the surface Fermi energy. However, when the model potential is applied to the system, the LUMO energy of the oxygen falls even lower with respect to the Fermi energy than what observed when using PBE.

Due to these unsatisfactory results, the project has been set aside and will not be published in its current form.

Chapter 8

Conclusions

In this dissertation a novel extension of subsystem density functional theory for molecular systems and the condensed phase is introduced.

The main output of this work is a new simulation package (eQE) which is based on the open-source Quantum Espresso. eQE is able to perform single point calculation and molecular dynamics at the subsystem DFT level in a plane wave basis set. In eQE the locality of the fragments is exploited to achieve maximum flexibility and efficiency: each fragment can have a specific basis set (through the introduction of auxiliary simulation cells), and a specific sampling of the first Brillouin zone. The parallel infrastructure of the package is found to be able to tackle simulation with thousands of atoms and processors, and its scaling is much closer to linearity than Kohn-Sham DFT.

The method has been tested against an array of systems, including molecules on surfaces, molecular liquids, and molecular crystals, and it is found to yield satisfactory results as long as the interactions between the fragments do not involve covalent bonds. This is due to known limitations of the readily available kinetic energy functionals that are used in the evaluation of the non-additive energy.

Finally, in a molecular dynamics study of liquid water, subsystem DFT has been found to be an effective practical tool. Quantum chemistry is based on error cancellation, and practical implementations of subsystem DFT (such as the one in eQE) show an improved model of liquids and radical species because the error in the nonadditive KEDF systematically cancels out the self-interaction error in the XC functional delivering results in quantitative agreement with the experiment and in turn, reality.

Bibliography

[1] CP2k: A General Program to Perform Molecular Dynamics Simulations. URL: http://www.cp2k.org.

[2] Carlo Adamo and Vincenzo Barone. Toward Reliable Density Functional Methods Without Adjustable Parameters: The PBE0 Model. *J. Chem. Phys.*, 110:6158–6170, 1999.

[3] Francesco Aquilante and Tomasz A. Wesolowski. Self-consistency in frozen-density embedding theory based calculations. *J. Chem. Phys.*, 135:084120, 2011.

[4] Volodymyr Babin, Claude Leforestier, and Francesco Paesani. Development of a "First Principles" Water Potential with Flexible Monomers: Dimer Potential Energy Surface, VRT Spectrum, and Second Virial Coefficient. *J. Chem. Theory Comput.*, 9:5395–5403, 2013.

[5] R. F. W. Bader. Everyman's Derivation of the Theory of Atoms in Molecules. *J. Phys. Chem.*, 19:8–29, 1980.

[6] A. Baldereschi. Mean-Value Point in the Brillouin Zone. *Phys. Rev. B*, 7:5212–5215, Jun 1973.

[7] D. Barker and M. Sprik. Molecular dynamics study of electron gas models for liquid water. *Mol. Phys.*, 101:1183, 2003.

[8] Charles W. Bauschlicher Jr. and Alessandra Ricca. On the interaction of CO and NH_3 with BHi_3 and BF_3. *Chem. Phys. Lett.*, 237:14–19, 1995.

[9] A. D. Becke. Density-functional exchange-energy approximation with correct asymptotic behavior. *Phys. Rev. A*, 38:3098–3100, 1988.

[10] Axel D. Becke. Density-functional thermochemistry. III. The role of exact exchange. *J. Chem. Phys.*, 98:5648–5652, 1993.

[11] J. Behler, Bernard Delley, Sönke Lorenz, K. Reuter, and M. Scheffler. Dissociation of O_2 at Al(111): The Role of Spin Selection Rules. *Phys. Rev. Lett.*, 94:036104, 2005.

[12] S. Maya Beyhan, Andreas W. Götz, and Lucas Visscher. Bond energy decomposition analysis for subsystem density functional theory. *J. Chem. Phys.*, 138:094113, 2013.

[13] F. Bloch. Bemerkung zur Elektronentheorie des Ferromagnetismus und der elektrischen Leitfähigkeit. *Z. Phys.*, 57:545–555, 1929.

[14] Peter E. Blöchl, O. Jepsen, and O. K. Andersen. Improved tetrahedron method for Brillouin-zone integrations. *Phys. Rev. B*, 49:16223–16233, Jun 1994.

[15] Carolyn S. Brauer, Galen Sedo, Erik M. Grumstrup, Kenneth R. Leopold, Mark D. Marshall, and Helen O. Leung. Effects of partially quenched orbital angular momentum on the microwave spectrum and magnetic hyperfine splitting in the OH-water complex. *Chem. Phys. Lett.*, 401:420–425, 2005.

[16] C. G. Broyden. A class of methods for solving nonlinear simultaneous equations. *Mathematics of Computation*, 19:577–577, 1965.

[17] Marten A. Buijse, Evert Jan Baerends, and Jaap G. Snijders. Analysis of correlation in terms of exact local potentials: Applications to two-electron systems. *Phys. Rev. A*, 40:4190–4202, 1989.

[18] Kieron Burke. Perspective on Density Functional Theory. *J. Chem. Phys.*, 136:150901, 2012.

[19] C. Carbogno, J. Behler, K. Reuter, and A. Groß. Signatures of nonadiabatic O_2 dissociation at Al(111): First-principles fewest-switches study. *Phys. Rev. B*, 81:035410, 2010.

[20] Wojciech Cencek and Krzysztof Szalewicz. On asymptotic behavior of density functional theory. *J. Chem. Phys.*, 139:024104, 2013.

[21] Wojciech Cencek and Krzysztof Szalewicz. Erratum: "On asymptotic behavior of density functional theory" [J. Chem. Phys. 139, 024104 (2013)]. *J. Chem. Phys.*, 140:149902, 2014.

[22] D. J. Chadi and Marvin L. Cohen. Special Points in the Brillouin Zone. *Phys. Rev. B*, 8:5747–5753, Dec 1973.

[23] Jeng-Da Chai and Martin Head-Gordon. Long-range corrected hybrid density functionals with damped atom–atom dispersion corrections. *Phys. Chem. Chem. Phys.*, 10:6615, 2008.

[24] Aron J. Cohen, Paula Mori-Sanchez, and Weitao Yang. Insights into Current Limitations of Density Functional Theory. *Science*, 321:792–794, 2008.

[25] Christopher J. Cramer and Donald G. Truhlar. Density functional theory for transition metals and transition metal chemistry. *Phys. Chem. Chem. Phys.*, 11:10757, 2009.

[26] Ernest R. Davidson. The Iterative Calculation of a Few of the Lowest Eigenvalues and Corresponding Eigenvectors of Large Real-Symmetric Matrices. *J. Comp. Phys.*, 17:87–94, 1975.

[27] Ernest R. Davidson. Super-matrix methods. *Computer Physics Communications*, 53(1):49–60, 1989.

[28] Robert A. DiStasio, Biswajit Santra, Zhaofeng Li, Xifan Wu, and Roberto Car. The individual and collective effects of exact exchange and dispersion interactions on the ab initio structure of liquid water. *J. Chem. Phys.*, 141:084502, 2014.

[29] Dale L. Doering and Theodore E. Madey. The adsorption of water on clean and oxygen-dosed ru(011). *Surface Science*, 123:305 – 337, 1982.

[30] Marcin Dułak, Jakub W. Kamiński, and Tomasz A. Wesołowski. Equilibrium Geometries of Noncovalently Bound Intermolecular Complexes Derived from Subsystem Formulation of Density Functional Theory. *J. Chem. Theory Comput.*, 3:735–745, 2007.

[31] Peter Elliott, Kieron Burke, Morrel H. Cohen, and Adam Wasserman. Partition Density-Functional Theory. *Phys. Rev. A*, 82:024501, 2010.

[32] See Supplementary Material Document No.[to be added] for additional tables and figures.

[33] R. A. Evarestov and V. P. Smirnov. Special points of the brillouin zone and their use in the solid state theory. *physica status solidi (b)*, 119(1):9–40, 1983.

[34] Enrico Fermi. Un Metodo Statistico per la Determinazione di alcune Prioprietà dell'Atomo. *Rend. Accad. Naz. Lincei*, 6:602–607, 1927.

[35] C. Fonseca Guerra, J. G. Snijders, G. te Velde, and E. J. Baerends. Towards an order-n dft method. *Theor. Chem. Acc.*, 99:391–403, 1998.

[36] Katrin Forster-Tonigold and Axel Groß. Dispersion corrected RPBE studies of liquid water. *J. Chem. Phys.*, 141:064501, 2014.

[37] Samuel Fux, Karin Kiewisch, Christoph R. Jacob, Johannes Neugebauer, and Markus Reiher. Analysis of Electron Density Distributions from Subsystem Density Functional Theory Applied to Coordination Bonds. *Chem. Phys. Lett.*, 461:353–359, 2008.

[38] Kevin F. Garrity, Joseph W. Bennett, Karin M. Rabe, and David Vanderbilt. Pseudopotentials for high-throughput DFT calculations. *Computational Materials Science*, 81:446–452, 2014.

[39] Alessandro Genova, Davide Ceresoli, Alisa Krishtal, Oliviero Andreussi, Robert A. DiStasio Jr., and Michele Pavanello. eQE — A Densitiy Functional Embedding Theory Code For The Condensed Phase. *Int. J. Quantum Chem.*, 117:e25401, 2017.

[40] Alessandro Genova, Davide Ceresoli, and Michele Pavanello. Periodic Subsystem Density-Functional Theory. *J. Chem. Phys.*, 141:174101, 2014.

[41] Alessandro Genova, Davide Ceresoli, and Michele Pavanello. Avoiding Fractional Electrons in Subsystem DFT Based Ab-Initio Molecular Dynamics Yields

Accurate Models For Liquid Water and Solvated OH Radical. *J. Chem. Phys.*, 144:234105, 2016.

[42] Alessandro Genova and Michele Pavanello. Exploiting the Locality of Subsystem Density Functional Theory: Efficient Sampling of the Brillouin Zone. *J. Phys.: Condens. Matter*, 27:495501, 2015.

[43] P Giannozzi, O Andreussi, T Brumme, O Bunau, M Buongiorno Nardelli, M Calandra, R Car, C Cavazzoni, D Ceresoli, M Cococcioni, N Colonna, I Carnimeo, A Dal Corso, S de Gironcoli, P Delugas, R A DiStasio Jr, A Ferretti, A Floris, G Fratesi, G Fugallo, R Gebauer, U Gerstmann, F Giustino, T Gorni, J Jia, M Kawamura, H-Y Ko, A Kokalj, E Küçükbenli, M Lazzeri, M Marsili, N Marzari, F Mauri, N L Nguyen, H-V Nguyen, A Otero de-la Roza, L Paulatto, S Poncé, D Rocca, R Sabatini, B Santra, M Schlipf, A P Seitsonen, A Smogunov, I Timrov, T Thonhauser, P Umari, N Vast, X Wu, and S Baroni. Advanced capabilities for materials modelling with q uantum espresso. *Journal of Physics: Condensed Matter*, 29(46):465901, 2017.

[44] Paolo Giannozzi, Stefano Baroni, Nicola Bonini, Matteo Calandra, Roberto Car, Carlo Cavazzoni, Davide Ceresoli, Guido L Chiarotti, Matteo Cococcioni, Ismaila Dabo, Andrea Dal Corso, Stefano de Gironcoli, Stefano Fabris, Guido Fratesi, Ralph Gebauer, Uwe Gerstmann, Christos Gougoussis, Anton Kokalj, Michele Lazzeri, Layla Martin-Samos, Nicola Marzari, Francesco Mauri, Riccardo Mazzarello, Stefano Paolini, Alfredo Pasquarello, Lorenzo Paulatto, Carlo Sbraccia, Sandro Scandolo, Gabriele Sclauzero, Ari P Seitsonen, Alexander Smogunov, Paolo Umari, and Renata M Wentzcovitch. QUANTUM ESPRESSO: a modular and open-source software project for quantum simulations of materials. *J. Phys.: Cond. Mat.*, 21:395502, 2009.

[45] André Severo Pereira Gomes, Christoph R. Jacob, and Lucas Visscher. Calculation of Local Excitations in Large Systems by Embedding Wave-Function Theory in Density-Functional Theory. *Phys. Chem. Chem. Phys.*, 10:5353–5362, 2008.

[46] Eneritz Muguruza González, Leonardo Guidoni, and Carla Molteni. Chemical and protein shifts in the spectrum of the photoactive yellow protein: a time-dependent density functional theory/molecular mechanics study. *Phys. Chem. Chem. Phys.*, 11:4556–4563, 2009.

[47] Jason D. Goodpaster, Nandini Ananth, Frederick R. Manby, and Thomas F. Miller, III. Exact Nonadditive Kinetic Potentials for Embedded Density Functional Theory. *J. Chem. Phys.*, 133:084103, 2010.

[48] Mark S. Gordon, Dmitri G. Fedorov, Spencer R. Pruitt, and Lyudmila V. Slipchenko. Fragmentation Methods: A Route to Accurate Calculations on Large Systems. *Chem. Rev.*, 112:632–672, 2012.

[49] A.W. Götz, S.M. Beyhan, and L. Visscher. Performance of Kinetic Energy Functionals for Interaction Energies in a Subsystem Formulation of Density Functional Theory. *J. Chem. Theory Comput.*, 5:3161–3174, 2009.

[50] N. Govind, Y. A. Wang, A. J. R. da Silva, and E. A. Carter. Accurate ab initio energetics of extended systems via explicit correlation embedded in a density functional environment. *Chem. Phys. Lett.*, 295:129–134, 1998.

[51] O. V. Gritsenko, P. R. T. Schipper, and E. J. Baerends. Approximation of the exchange–correlation Kohn–Sham potential with a statistical average of different orbital model potentials. *Chem. Phys. Let.*, 302:199–207, 1999.

[52] Oleg Gritsenko and Evert Jan Baerends. Asymptotic correction of the exchange correlation kernel of time-dependent density functional theory for long-range charge-transfer excitations. *J. Chem. Phys.*, 121:655–660, 2004.

[53] Oleg V. Gritsenko. On the Principal Difference Between the Exact and Approximate Frozen-Density Embedding Theory. In Tomasz A. Wesolowski and Yan Alexander Wang, editors, *Recent Advances in Orbital-Free Density Functional Theory*, chapter 12, pages 355–365. World Scientific, Singapore, 2013.

[54] M. Grüning, O. V. Gritsenko, S. J. A. van Gisbergen, and E. J. Baerends. On the required shape corrections to the local density and generalized gradient approximations to the Kohn–Sham potentials for molecular response calculations of (hyper-) polarizabilities and excitation energies. *J. Chem. Phys.*, 116:9591, 2002.

[55] Michael P. Guse. An atoms in molecules approach to density functional theory. *J. Chem. Phys.*, 75:828–833, 1981.

[56] Jochen Heyd, Gustavo E. Scuseria, and Matthias Ernzerhof. Erratum: "hybrid functionals based on a screened coulomb potential" [j. chem. phys. 118, 8207 (2003)]. *The Journal of Chemical Physics*, 124(21):219906, 2006.

[57] F. L. Hirshfeld. Bonded-Atom Fragments For Describing Molecular Charge-Densities. *Theor. Chem. Acc.*, 44:129–138, 1977.

[58] Miroslav Hodak, Wenchang Lu, and J. Bernholc. Hybrid *ab initio* Kohn–Sham density functional theory/frozen-density orbital-free density functional theory simulation method suitable for biological systems. *J. Chem. Phys.*, 128:014101, 2008.

[59] P. Hu, D.A. King, M.-H. Lee, and M.C. Payne. Orbital mixing in {CO} chemisorption on transition metal surfaces. *Chemical Physics Letters*, 246(1–2):73–78, 1995.

[60] Congcong Huang, K. T. Wikfeldt, D. Nordlund, U. Bergmann, T. McQueen, J. Sellberg, L. G. M. Pettersson, and A. Nilsson. Wide-angle X-ray diffraction and molecular dynamics study of medium-range order in ambient and hot water. *Phys. Chem. Chem. Phys.*, 13:19997, 2011.

[61] Marcella Iannuzzi, Barbara Kirchner, and Jürg Hutter. Density Functional Embedding for Molecular Systems. *Chem. Phys. Lett.*, 421:16–20, 2006.

[62] Christoph R. Jacob and Johannes Neugebauer. Subsystem density-functional theory. *WIREs: Comput. Mol. Sci.*, 4:325–362, 2014.

[63] Christoph R. Jacob, Johannes Neugebauer, and Lucas Visscher. A Flexible Implementation of Frozen-Density Embedding for Use in Multilevel Simulations. *J. Comput. Chem.*, 29:1011–1018, 2008.

[64] Christoph R. Jacob and Lucas Visscher. Density–functional theory approach for the quantum chemical treatment of proteins. *J. Chem. Phys.*, 128:155102, 2008.

[65] R. Kevorkyants, M. Dulak, and T. A. Wesolowski. Interaction energies in hydrogen-bonded systems: A testing ground for subsystem formulation of density-functional theory. *J. Chem. Phys.*, 124:024104, 2006.

[66] Ruslan Kevorkyants, Henk Eshuis, and Michele Pavanello. FDE-vdW: A van der Waals Inclusive Subsystem Density-Functional Theory. *J. Chem. Phys.*, 141:044127, 2014.

[67] Ruslan Kevorkyants, Xiqiao Wang, David M. Close, and Michele Pavanello. Calculating Hyperfine Couplings in Large Ionic Crystals Containing Hundreds of QM Atoms: Subsystem DFT is the Key. *J. Phys. Chem. B*, 117:13967–13974, 2013.

[68] Rustam Z. Khaliullin, Alexis T. Bell, and Martin Head-Gordon. Electron Donation in the Water-Water Hydrogen Bond. *Chemistry - A European Journal*, 15:851–855, 2008.

[69] Rustam Z. Khaliullin and Thomas D. Kühne. Microscopic properties of liquid water from combined ab initio molecular dynamics and energy decomposition studies. *Phys. Chem. Chem. Phys.*, 15:15746, 2013.

[70] Karin Kiewisch, Georg Eickerling, Markus Reiher, and Johannes Neugebauer. Topological analysis of electron densities from Kohn–Sham and subsystem density functional theory. *J. Chem. Phys.*, 128:044114, 2008.

[71] W. Kohn and L. J. Sham. Self-Consistent Equations Including Exchange and Correlation Effects. *Phys. Rev.*, 140:1133–1138, 1965.

[72] Arseny Kovyrshin and Johannes Neugebauer. Analytical gradients for excitation energies from frozen-density embedding. *Phys. Chem. Chem. Phys.*, 2016.

[73] Alisa Krishtal, Debalina Sinha, Alessandro Genova, and Michele Pavanello. Subsystem Density-Functional Theory as an Effective Tool for Modeling Ground and Excited States, their Dynamics, and Many-Body Interactions. *J. Phys.: Condens. Matter*, 27:183202, 2015.

[74] Thomas D. Kühne, Matthias Krack, and Michele Parrinello. Static and Dynamical Properties of Liquid Water from First Principles by a Novel Car-Parrinello-like Approach. *J. Chem. Theory Comput.*, 5:235–241, 2009.

[75] D. Lahav and T. Klüner. A self-consistent density based embedding scheme applied to the adsorption of co on pd(111). *J. Phys.: Condens. Matter*, 19(22):226001, 2007.

[76] David C. Langreth and John P. Perdew. The exchange-correlation energy of a metallic surface. *Solid State Commun.*, 17:1425–1429, 1975.

[77] S. Laricchia, E. Fabiano, L. A. Constantin, and F. Della Sala. Generalized Gradient Approximations of the Noninteracting Kinetic Energy from the Semiclassical Atom Theory: Rationalization of the Accuracy of the Frozen Density Embedding Theory for Nonbonded Interactions. *J. Chem. Theory Comput.*, 7:2439–2451, 2011.

[78] S. Laricchia, E. Fabiano, and F. Della Sala. Frozen density embedding with hybrid functionals. *J. Chem. Phys.*, 133:164111, 2010.

[79] Hee-Seung Lee and Mark E. Tuckerman. Dynamical properties of liquid water from ab initio molecular dynamics performed in the complete basis set limit. *J. Chem. Phys.*, 126(16):164501, 2007.

[80] A. Lembarki and H. Chermette. Obtaining a Gradient-Corrected Kinetic-Energy Functional from the Perdew-Wang Exchange Functional. *Phys. Rev. A*, 50:5328, 1994.

[81] Florian Libisch, Chen Huang, Peilin Liao, Michele Pavone, and Emily A. Carter. Origin of the Energy Barrier to Chemical Reactions of O_2 on Al(111): Evidence for Charge Transfer, Not Spin Selection. *Phys. Rev. Lett.*, 109:198303, 2012.

[82] Heng-Rui Liu, Hongjiun Xiang, and X.G. Gong. First Principles Study of Adsorption of O_2 on Al Surface with Hybrid Functionals. *J. Chem. Phys.*, 135:214702, 2011.

[83] Ester Livshits, Roi Baer, and Ronnie Kosloff. Deleterious Effects of Long-Range Self-Repulsion on the Density Functional Description of O_2 on Aluminium. *J. Phys. Chem. A*, 113:7521, 2009.

[84] Sandra Luber. Local electric dipole moments for periodic systems via density functional theory embedding. *J. Chem. Phys.*, 141:234110, 2014.

[85] Marcus Lundberg and Per E. M. Siegbahn. Quantifying the effects of the self-interaction error in DFT: When do the delocalized states appear? *J. Chem. Phys.*, 122:224103, 2005.

[86] M Lynch and P Hu. A density functional theory study of {CO} and atomic oxygen chemisorption on Pt(111). *Surface Science*, 458(1–3):1–14, 2000.

[87] G. Makov, R. Shah, and M. C. Payne. Periodic boundary conditions in *ab initio* calculations. II. Brillouin-zone sampling for aperiodic systems. *Phys. Rev. B*, 53:15513–15517, Jun 1996.

[88] F. R. Manby and P. J. Knowles. Poisson equation in the kohn-sham coulomb problem. *Phys. Rev. Lett.*, 87:163001, Sep 2001.

[89] Dominik Marx and Juerg Hutter. *Ab Initio Molecular Dynamics*. Cambridge University Press, 2009. http://www.cambridge.org/gb/knowledge/isbn/item2327682/.

[90] Sheng Meng, E. G. Wang, and Shiwu Gao. Water adsorption on metal surfaces: A general picture from density functional theory studies. *Phys. Rev. B*, 69:195404, 2004.

[91] M. Methfessel and A. T. Paxton. High-precision sampling for brillouin-zone integration in metals. *Phys. Rev. B*, 40:3616–3621, 1989.

[92] Hendrik J. Monkhorst and James D. Pack. Special points for Brillouin-zone integrations. *Phys. Rev. B*, 13:5188–5192, 1976.

[93] Juana Moreno and José M. Soler. Optimal meshes for integrals in real- and reciprocal-space unit cells. *Phys. Rev. B*, 45:13891–13898, Jun 1992.

[94] P.S. Moussounda, M.F. Haroun, B. M'Passi-Mabiala, and P. Legare. A dft investigation of methane molecular adsorption on pt(100). *Surf. Sci.*, 594:231 – 239, 2005.

[95] Jonathan Nafziger and Adam Wasserman. Density-Based Partitioning Methods for Ground-State Molecular Calculations. *J. Phys. Chem. A*, 118:7623–7639, 2014.

[96] Jonathan Nafziger and Adam Wasserman. Fragment-based treatment of delocalization and static correlation errors in density-functional theory. *J. Chem. Phys.*, 143:234105, 2015.

[97] Hiroya Nakata, Dmitri G. Fedorov, Kazuo Kitaura, and Shinichiro Nakamura. Extension of the fragment molecular orbital method to treat large open-shell systems in solution. *Chem. Phys. Lett.*, 635:86–92, 2015.

[98] Hiroya Nakata, Dmitri G. Fedorov, Satoshi Yokojima, Kazuo Kitaura, and Shinichiro Nakamura. Derivatives of the approximated electrostatic potentials in unrestricted Hartree–Fock based on the fragment molecular orbital method and an application to polymer radicals. *Theor. Chem. Acc.*, 133, 2014.

[99] Roman F. Nalewajski and Robert G. Parr. Information theory, atoms in molecules, and molecular similarity. *Proc. Natl. Acad. Sci. USA*, 97:8879–8882, 2000.

[100] Robert G. Parr and Weitao Yang. *Density-Functional Theory of Atoms and Molecules*. Oxford University Press, Oxford, 1989.

[101] Michele Pavanello and Johannes Neugebauer. Modelling Charge Transfer Reactions with the Frozen Density Embedding Formalism. *J. Chem. Phys.*, 135:234103, 2011.

[102] Michele Pavanello, Troy Van Voorhis, Lucas Visscher, and Johannes Neugebauer. An Accurate and Linear-Scaling Method for Calculating Charge-Transfer Excitation Energies and Diabatic Couplings. *J. Chem. Phys.*, 138:054101, 2013.

[103] J. P. Perdew. Generalized gradient approximation for the fermion kinetic energy as a functional of the density. *Phys. Lett. A*, 165:79–82, 1992.

[104] J. P. Perdew and A. Zunger. Self-Interaction Correction To Density-Functional Approximations For Many-Electron Systems. *Phys. Rev. B*, 23:5048, 1981.

[105] John P. Perdew, Kieron Burke, and Matthias Ernzerhof. Generalized Gradient Approximation Made Simple. *Phys. Rev. Lett.*, 77:3865–3868, 1996.

[106] John P. Perdew, Matthias Ernzerhof, and Kieron Burke. Rationale for mixing exact exchange with density functional approximations. *J. Chem. Phys.*, 105:9982, 1996.

[107] Peter Pulay. Convergence Acceleration of Iterative Sequences. The Case of SCF Iteration. *Chem. Phys. Lett.*, 73:393–398, 1980.

[108] Pablo Ramos, Mark Mankarious, and Michele Pavanello. A Critical Look at Methods for Calculating Charge Transfer Couplings Fast and Accurately. In *Practical Aspects in Computational Chemistry IV*. Springer, 2016. Chapter 4.

[109] Pablo Ramos and Michele Pavanello. Quantifying Environmental Effects on the Decay of Hole Transfer Couplings in Biosystems. *J. Chem. Theory Comput.*, 10:2546–2556, 2014.

[110] Pablo Ramos and Michele Pavanello. Performance of Frozen Density Embedding for Modeling Hole Transfer Reactions. *J. Phys. Chem. B*, 119:7541–7557, 2015.

[111] Simen Reine, Trygve Helgaker, and Roland Lindh. Multi-electron integrals. *WIREs: Comput. Mol. Sci.*, 2:290–303, 2012.

[112] R. Resta and D. Vanderbilt. Theory of polarization: A modern approach. In *Physics of Ferroelectrics: a Modern Perspective, Topics in Applied Physics*, volume 105, page 31. Springer-Verlag, 2007.

[113] I J Robertson and M C Payne. k-point sampling and the k.p method in pseudopotential total energy calculations. *Journal of Physics: Condensed Matter*, 2(49):9837, 1990.

[114] I. Roeggen and Tor Johansen. Cholesky decomposition of the two-electron integral matrix in electronic structure calculations. *J. Chem. Phys.*, 128:194107, 2008.

[115] Tobias Schmidt, Eli Kraisler, Leeor Kronik, and Stephan Kümmel. One-electron self-interaction and the asymptotics of the Kohn–Sham potential: an impaired relation. *Phys. Chem. Chem. Phys.*, 16:14357–14367, 2014.

[116] A. Seidl, A. Görling, P. Vogl, J. A. Majewski, and M. Levy. Generalized Kohn-Sham schemes and the band-gap problem. *Phys. Rev. B*, 53:3764–3774, 1996.

[117] Lawrie B. Skinner, Congcong Huang, Daniel Schlesinger, Lars G. M. Pettersson, Anders Nilsson, and Chris J. Benmore. Benchmark oxygen-oxygen pair-distribution function of ambient water from x-ray diffraction measurements with a wide Q-range. *J. Chem. Phys.*, 138:074506, 2013.

[118] Alisa Solovyeva, Michele Pavanello, and Johannes Neugebauer. Spin Densities from Subsystem Density-Functional Theory: Assessment and Application to a Photosynthetic Reaction Center Complex Model. *J. Chem. Phys.*, 136:194104, 2012.

[119] Alisa Solovyeva, Michele Pavanello, and Johannes Neugebauer. Describing long-range charge-separation processes with subsystem density-functional theory. *J. Chem. Phys.*, 140:164103, 2014.

[120] A. K. Soper and C. J. Benmore. Quantum Differences between Heavy and Light Water. *Phys. Rev. Lett.*, 101, 2008.

[121] Jon M. Sorenson, Greg Hura, Robert M. Glaeser, and Teresa Head-Gordon. What can x-ray scattering tell us about the radial distribution functions of water? *J. Chem. Phys.*, 113:9149, 2000.

[122] Tamar Stein, Leeor Kronik, and Roi Baer. Prediction of charge-transfer excitations in coumarin-based dyes using a range-separated functional tuned from first principles. *J. Chem. Phys.*, 131:244119, 2009.

[123] P. J. Stephens, F. J. Devlin, C. F. Chabalowski, and M. J. Frisch. *Ab initio* Calculation of Vibrational Adsorption and Circular Dichroism Spectra Using Density Functional Force Fields. *J. Chem. Phys.*, 98:11623–11627, 1994.

[124] David G. Tempel, Todd J. Martínez, and Neepa T. Maitra. Revisiting Molecular Dissociation in Density Functional Theory: A Simple Model. *J. Chem. Theory Comput.*, 5:770–780, 2009.

[125] R. van Leeuwen and E. J. Baerends. An exchange–correlation potential with correct asymptotic behaviour. *Phys. Rev. A*, 49:2421–2431, 1994.

[126] David Vanderbilt. Soft self-consistent pseudopotentials in a generalized eigenvalue formalism. *Phys. Rev. B*, 41:7892–7895, 1990.

[127] J. VandeVondele and M. Sprik. A Molecular Dynamics Study of the Hydroxyl Radical in Solution Applying Self-Interaction-Corrected Density Functional Methods. *Phys. Chem. Chem. Phys.*, 7:1363–1367, 2005.

[128] P. Vassilev, M. J. Louwerse, and E. J. Baerends. Ab initio molecular dynamics simulation of the OH· radical in liquid water. *Chem. Phys. Lett.*, 398:212–216, 2004.

[129] S. H. Vosko, L. Wilk, and M. Nusair. Accurate spin-dependent electron liquid correlation energies for local spin density calculations: a critical analysis. *Can. J. Phys.*, 58:1200–1211, 1980.

[130] T. A. Wesolowski. Density functional theory with approximate kinetic energy functionals applied to hydrogen bonds. *J. Chem. Phys.*, 106:8516–8526, 1997.

[131] T. A. Wesolowski. One-Electron Equations for Embedded Electron Density: Challenge for Theory and Practical Payoffs in Multi-Level Modeling of Complex Polyatomic Systems. In J. Leszczynski, editor, *Computational Chemistry: Reviews of Current Trends*, volume 10, pages 1–82. World Scientific, Singapore, 2006.

[132] T. A. Wesolowski, A. Goursot, and J. Weber. Properties of CO adsorbed in ZSM5 zeolite: Density functional theory study using the embedding scheme based on electron density partitioning. *J. Chem. Phys*, 115:4791–4797, 2001.

[133] T. A. Wesolowski, O. Parisel, Y. Ellinger, and J. Weber. Comparative Study of Benzene$\cdots$X (X = O_2, N_2, CO) Complexes Using Density Functional Theory: The Importance of an Accurate Exchange–Correlation Energy Density at High Reduced Density Gradients. *J. Phys. Chem. A*, 101:7818–7825, 1997.

[134] T. A. Wesolowski and A. Warshel. Frozen Density Functional Approach for *ab Initio* Calculations of Solvated Molecules. *J. Chem. Phys.*, 97:8050, 1993.

[135] T. A. Wesolowski and J. Weber. Kohn-Sham Equations with Constrained Electron Density: An Iterative Evaluation of the Ground-State Electron Density of Interacting Molecules. *Chem. Phys. Lett.*, 248:71–76, 1996.

[136] Tomasz A. Wesolowski, Sapana Shedge, and Xiuwen Zhou. Frozen-Density Embedding Strategy for Multilevel Simulations of Electronic Structure. *Chem. Rev.*, 115:5891–5928, 2015.

[137] Qin Wu and Troy Van Voorhis. Direct optimization method to study constrained systems within density-functional theory. *Phys. Rev. A*, 72:024502, 2005.

[138] Qin Wu and Troy Van Voorhis. Extracting electron transfer coupling elements from constrained density functional theory. *J. Chem. Phys.*, 125:164105, 2006.